Engineering

Journal of Research

of the

U.S. National Bureau of Standards

JANUARY 1954

VOLUME [illegible] NUMBER 1

U. S. DEPARTMENT OF COMMERCE
Charles Sawyer, Secretary
NATIONAL BUREAU OF STANDARDS
A. V. Astin, Director

JANUARY 1954
VOLUME 52
NUMBER 1

JOURNAL OF RESEARCH

of the

NATIONAL BUREAU OF STANDARDS

PERIODICALS OF THE NATIONAL BUREAU OF STANDARDS

The National Bureau of Standards is engaged in fundamental and applied research in physics, chemistry, mathematics, and engineering. Projects are conducted in thirteen fields: electricity, optics and metrology, heat and power, atomic and radiation physics, chemistry, mechanics, organic and fibrous materials, metallurgy, mineral products, building technology, applied mathematics, electronics, and radio propagation. The Bureau has custody of the national standards of measurement and conducts research leading to the improvement of scientific and engineering standards and of techniques and methods of measurement. Testing methods and instruments are developed; physical constants and properties of materials are determined; and technical processes are investigated.

JOURNAL OF RESEARCH

Internationally known as a leading scientific periodical, the Journal presents research papers by authorities in the specialized fields of physics, mathematics, chemistry, and engineering. Complete details of the work are published, including laboratory data, experimental procedures, and theoretical and mathematical analyses. Annual subscription: domestic, $5.50; foreign, $7.75.

TECHNICAL NEWS BULLETIN

Summaries of current research at the National Bureau of Standards are published each month in the Technical News Bulletin. The articles are brief, with emphasis on the purpose of research, chosen on the basis of wide interest or technologic importance. Lists of all Bureau publications during the preceding month are given, including Research Papers, Handbooks, Applied Mathematics Series, Building Materials and Structures Reports, and Circulars. Each issue contains 12 or more two-column pages; illustrated. Annual subscription: domestic, $1.00; foreign, $1.25.

[illegible] RADIO PROPAGATION PREDICTIONS

The Predicted [illegible] necessary [illegible] the best [illegible] for communication between [illegible] the world at any time, [illegible] month. [illegible] important [illegible] communications and [illegible] investigators of [illegible] three months in [illegible] 10 [illegible] Annual subscription: [illegible]

Order publications from [illegible]
U. S. Government Printing [illegible]
[illegible] approved [illegible]

Journal of Research of the National Bureau of Standards Vol. 52, No. 1, January 1954 Research Paper 2464

Apparatus for the Determination of Minor Components of a Gas Mixture

Martin Shepherd†

The apparatus is primarily for the determination of the components occurring in low partial pressures in a gas mixture, and which ordinarily cannot be determined with satisfactory accuracy because of the significant sorption and desorption of major components in the reagents intended for the removal of the minor ones. Small amounts of solid and liquid reagents are used in the apparatus, and combustions, as well as absoprptions, can be performed. The apparatus can be made a separate unit or part of a standard apparatus for volumetric chemical gas analysis.

1. Introduction

There comes a time in the life of every exasperated gas analyst when he tires of cleaning liquid reagents from parts of the apparatus not intended to contain them, and the tendency of solutions to wander out of bounds prompts the desire to substitute less nomadic solid reagents. And there are times when the analyst is discouraged by conventional analyses that have indicated minor constituents that did not exist in the samples analyzed, or lost small but significant portions of major constituents. Errors caused by the solubility of components in a reagent not intended for their removal have long been a problem in gas analysis. During 1938 the apparatus described here was designed to eliminate such errors of solubility, at least within the significance of the better volumetric systems. Prior to this, the idea had been used in determining carbon dioxide in air captured in the stratosphere [1],[1] and for the determination of ethylene oxide in carbon dioxide [2]. Part of this apparatus was illustrated and briefly mentioned in a paper [3] describing modifications of what was then our volumetric gas analysis apparatus.

The determination of constituents of small partial pressures has been successfully done by Bone and Wheeler, whose apparatus seems to be one of the standard types used in England [4]. This apparatus requires the addition of a small amount of fresh reagent for each absorption conducted, and while this minimizes the errors of solubility associated with the ordinary volumetric apparatus (usually referred to as an Orsat), this gain in accuracy is obtained by a considerable inconvenience in operation. Analysts in general have shown too great an impatience ever to accept the Bone and Wheeler procedure. So they have put up with errors of solubility.

Errors caused by solubility have long been recognized and even talked about, but it took a demonstration like the cooperative analysis of a sample of natural gas by 30 laboratories working with Subcommittee D–3–VII (Analysis of Gaseous Fuels) of the American Society for Testing Materials to bring a full realization of the magnitude of these errors [5]. The determination of oxygen was particularly interesting because there was no significant amount of oxygen in the sample. One- or two-tenths of a percent of oxygen is usually reported in the analysis of a natural gas, and the extent to which oxygen really does occur has long been a question. Of 294 analyses reported, 124 (only 42 percent) correctly indicated no oxygen; 58 (about 20 percent) indicated 0.1 percent of oxygen, which may be considered the average error of solubility that experience has shown may be expected; and 69 (about 23 percent) indicated 0.2 percent of oxygen, which should have been the maximum error caused by solubility alone. However, 24 and 19 analyses indicated 0.3 and 0.4 percent, respectively, and these values round off a probability curve.

Errors of solubility can be minimized by using small amounts of solid reagents and liquid reagents in reaction tubes designed to confine them. The reaction tubes can be connected to the distributor of the gas analysis apparatus in such a way that the manipulations involved are more easily performed than in the case with the ordinary volumetric apparatus employing liquids in pipet. Actually, the reaction tubes form an integral part of the distributor, and a reaction is conducted by simply passing gas from the buret through the tube and into a reservoir over mercury, just as though the gas were being passed through the distributor itself.

The apparatus can be made a separate unit or a part of the conventional gas analysis apparatus.

2. The Separate Unit

The separate unit is independent of the regular one ordinarily used for volumetric analysis. It is possible to do a complete absorption-combustion analysis with this unit, even with gases of average composition, but it is primarily intended for the determination of components of a mixture that occur in small amounts. If the type of analysis performed requires the determination of components present in both large and small amounts, the apparatus described in section 3 is the one to use.

The various reaction tubes of this unit are permanently sealed to the distributor, which may be made in 1, 2, or 3 sections, as desired. A natural

† Deceased, September 17, 1953.

[1] Figures in brackets indicate the literature references at the end of this paper.

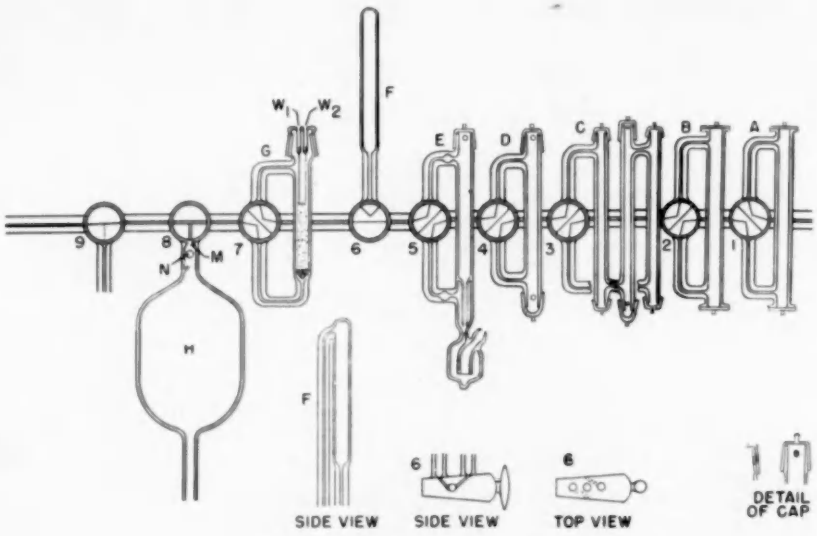

FIGURE 1. *Separate unit.*

division would be to include absorption tubes in one section (see fig. 1, stopcocks 1 to 5, inclusive), combustion tubes in a second (cocks 6 and 7), and the reservoir and connection for the pipet containing alkaline pyrogallol solution in the third (cocks 8 and 9). In arranging the section for absorptions, the particular needs of the work to be done will often indicate a simplification of the apparatus shown.

If the distributor is made in a single section, the total length (60 cm) makes it advisable to use 10-mm outside diameter capillary tubing for the horizontal member, and the vertical members are 8-mm outside diameter, and all bores are 2 mm. When the distributor is divided, the sections are connected with 12/2 interchangeable spherical joints, such as terminate the distributor at both ends.

The buret used with this unit is not shown, but is just like the one previously described [6], complete with the special compensator-manometer, except that the top 45 ml of the buret itself is a pear-shaped bulb. The stem of the buret is graduated in the standard manner [6], but as the over-all length is the same and the volume only half that of the regular buret, the stem may be marked in intervals of 0.1 ml rather than 0.2 ml, which is advantageous for analysis of this kind, and the standard water jacket and frame may be used.

As previously noted, the reaction tubes are integral parts of the distributor and are designed to use small amounts of either solid or liquid reagents. They are connected by stopcocks with keys bored so that in one position the reaction tube is bypassed, and in another position gas from the buret enters the bottom of the reaction tube and leaves the top traveling left into the distributor on its way to the mercury-filled reservoir. The various tubes will be briefly described.

Reaction tubes A and B (fig. 1) are alike, and are for solid reagents. The ends of these tubes are closed with flat caps ground to fit the ground flat flanges at the top and bottom of the tubes. These joints may be sealed with a low-melting thermoplastic cement or with a heavy lubricant. The caps have glass spurs to hold retaining springs or rubber bands in place. These tubes are ordinarily used with a desiccant, such as phosphorous pentoxide on glass wool or calcium sulfate, in the event a dry analysis is done; or with Ascarite for the removal of carbon dioxide and other acid gases.

Reaction tube C may be used with solid reagents, or the central tube may be used with a liquid reagent on glass wool while the outer tubes contain solid reagents. For example, a few drops of fuming sulfuric acid in the middle tube, and a packing of glass wool and Ascarite in the outer tubes, may be used to determine small amounts of unsaturated hydrocarbons in fuel gases; or calcium sulfate in the outer tubes and Hopcalite in the middle tube will serve to remove small amounts of carbon monoxide from the gas sample. When a liquid reagent is used in the central tube it is introduced through holes in the top cap and top male grinding of the tube, which may be made to coincide by rotating the cap. For convenience in filling, the open position is at the front of the tube, and the holes are drilled at a downward angle (fig. 1) to permit insertion of the nozzle of a medicine dropper, from which the reagent is transferred. The excess and spent reagents are removed through a similar arrangement at the bottom of the tube, again using the medicine dropper. Dropping bottles may be used for the convenient storage of reagents.

Tube D is for liquid reagents, and is like the middle tube of C except for internal diameter. Glass wool

or glass tape is ordinarily used as a packing to hold solutions. The diameter of this tube will permit another packing—a central glass rod wound with a helix of glass wicking, which snugly fills the annular space, thus providing a relatively long path for the gas to travel.

Tube E is designed to permit coating the packing with fresh reagent several times during an absorption. One charge of reagent may also last for quite a few analyses. The solution is placed in the lower reservoir and forced up over the packing by compressing a rubber bulb attached to the top outlet of this reservoir. The in-seal tube just above the reservoir allows the solution to ascend the reaction tube without entering the left-hand capillary to stopcock 5 (which is closed during this procedure). The solution is brought to an etched mark on the neck just above the reservoir (before each gas volume is measured) by a screw clamp on the rubber bulb attached at the top of the reservoir.

Tube F is for combustion with a catalyst heated by an outer tube furnace. Copper oxide is ordinarily used.

Tube G is a combustion tube containing a platinum helix fastened to two platinum leads of much larger diameter than the helix. Contact to power leads is made through two mercury-filled wells (W_1, W_2) in the top cap. This cap is fastened to the combustion tube with a high-melting thermoplastic cement, and is cooled with strong air jets during a combustion. A packing of fine quartz sand acts as a safe flashback trap. The combustible gases are premixed with oxygen before burning.

Tube H is a mercury-filled reservoir, which confines the gases passed through the reaction tubes, and delivers them back to the buret. For convenience in displacing gas from the reservoir, a ground spherical ball N fits against ground 45-degree seat M. The seat is ground snugly into the bottom lead of the T-cock 8, presenting essentially no dead space. The ball cuts off the flow of mercury as the gas is delivered from the reservoir with a volumetric reproducibility better than could be obtained by adjustment to an etched mark, and with far greater ease.

A pipet of the distributor-tip type [7] is connected to stopcock 9. This furnishes the nitrogen necessary as a flushing, or sweeping, gas used to transfer the sample as required throughout the apparatus.

3. Procedure for an Analysis With the Separate Unit

3.1. Preparation of Transfer Gas

The sweeping or transfer gas that may be needed is prepared by absorbing oxygen from air, and storing over the alkaline pyrogallol solution in the pipet connected to stopcock 9. The recently developed pyro solution should be used [8]. The distributor, all reaction tubes, and the arm of the manometer connected to the distributor are adjusted to the reference compensator pressure.

3.2. Procedure for an Absorption With Solid Reagents

The gas sample is measured and then transferred at the approximate rate of 100 ml/min through the first reaction tube (with all other tubes bypassed) to the reservoir H. The gas contained in the arm of the manometer connected to the distributor is displaced into the buret, and then transferred through the reaction tube. If it is important to keep the reagent at the exit of the reaction tube fresh, the residual gas is returned from the reservoir to the buret with the reaction tube bypassed, but if the condition of the reagent at the exit of the reaction is not important, the residual gas is returned through the tube. The cycle is repeated until all significant reaction has occurred as shown by no further contraction. The pressure in the buret, distributor, and reaction tube are adjusted to the reference pressure, and the volume of the residual gas is measured.

3.3. Procedure for Absorption With Liquid Reagents

When the nitrogen is prepared at the beginning of the analysis, and all reaction tubes are filled with it, the liquid reagents to be used are introduced at the top of each of the reaction tubes designed to contain them. A very slow flow of nitrogen from the buret will prevent air from entering the reaction tube during introduction of the solution, but if there is any reason to suspect air contamination, a few final passages into the pyrogallol may be made. The final nitrogen balance is made after the introduction of the liquid reagents. The actual procedure for absorptions is the same as that outlined for absorptions with solid reagents.

3.4. Procedure for Combustion

The procedure for combustion with copper oxide does not differ from the routine ordinarily described. Inasmuch as carbon dioxide, which may be produced, is strongly absorbed on a cooling catalyst, it is best to start and stop with the catalyst hot. The initial nitrogen balance should be made with this in mind.

The combustion over the hot platinum helix is apt to be more complete than the conventional slow combustion. The residual sample from the absorption analysis is stored in the reservoir while the oxygen (or air) for the combustion is measured. These two gases are mixed by passing back and forth between reservoir and buret, and then the mixture is passed over the glowing platinum helix and thence through the flashback trap to the reservoir at the approximate rate of 20 ml/min. The gas in the arm of the manometer connected to the distributor is displaced and passed through the combustion tube. After this, the residual mixture in the reservoir may be below the explosive limit, and this gas may be passed back over the platinum to the buret. However, the safety of this procedure should be established by experience. The cycle is continued until no further significant reaction occurs. Carbon diox-

ide in the products of combustion is absorbed in Ascarite contained in one of the reaction tubes. In some analyses it is advantageous to absorb the carbon dioxide during the combustion procedures. For example, methane and ethane (and other hydrocarbons) calculated from contraction and carbon dioxide produced are seriously in error, whereas calculation from contraction, carbon dioxide produced, and oxygen consumed, will give more accurate results [9]. In such cases, the removal of carbon dioxide during the course of the combustion will result in a more rapid and possibly more complete combustion.

3.5. General Procedure

When the gas sample, or a part of it, has entered a reaction tube, some of the residue remaining in the tube is reactive with respect to the rest of the analysis. It is obvious that with each successive reaction the gas in formerly used tubes must enter the tube used for each new reaction. Bringing all the gas into the reactive zone is quite easily done with this apparatus. In the more conventional volumetric apparatus, passing the gas into a succession of absorption pipets or correcting for reactive residues by the calibrated distributor procedure [6] is considerably more trouble.

The apparatus must be operated in an area of reasonably constant temperature. One single reaction tube when filled with reagent contains about 3.5 ml of gas, so that an error of about 0.01 ml/deg C change in temperature could be made in comparing volumes before and after an absorption. The error with a double or triple reaction tube would be almost proportionately greater. The accumulative error for a complete analysis, using every reaction pipet shown, would be about 0.2 ml/deg C. This is too great, and temperature corrections should be applied if the laboratory is not suitably conditioned. The volumes of the various reaction tubes are easily determined by evacuation and subsequent filling from the buret. For more accurate work involving very small changes in volume, reaction tubes of smaller volume than those shown should be used. As this apparatus is likely to be put to special uses, it should be tailored to fit.

4. Reaction Tubes Adapted to Standard Volumetric Apparatus

The average analytical demand may not require a complete separate unit of the kind just described. Instead, the standard volumetric apparatus will usually be employed for the analysis of most gas mixtures, but as most mixtures are apt to contain one or more components in small percentages, the reaction tubes might well be employed for part of the analysis. Fortunately, they are neatly adaptable to the standard apparatus. This may be done with a set of special connectors and interchangeable spherical ground-glass joints. The reaction tubes may be connected across 2 T-cocks of a distributor, or better yet, to one cock of the type designed to pass gas into and out of a closed tube, or bypass the tube. Such units are commercially available. These reaction tubes, their connectors, and the distributor section designed for them are shown in figures 2, 3, and 4. The connectors and the basic reaction tube for solids or liquids upon glass wool or tape are shown in figure 2. The tube itself is shown at A. With connector D it forms a single reaction tube that fits the outlets of the special distributor stopcock shown at G, figure 4. With connector C, two of A make a double reaction tube, and with connector B and another of A added to the double tube, a triple reaction tube is assembled. The special tube for absorptions requiring several applications of fresh reagent is shown at F, figure 3; its connector is F of figure 2. The slow-combustion tube is shown at G, figure 3; its connector is G of figure 2. The copper-oxide tube is shown at H, figure 3; it needs no connector unless keyed into two T-cocks of a standard distributor, in which case two of connector H (fig. 2) will serve to bring it to the proper upward position. The mercury-filled reservoir, K of figure 3 may be connected to a T-cock of the standard distributor if space permits, but the combustion pipet of the standard apparatus will serve for this reservoir, albeit not so neatly. Figure 4 shows a five-cock standard distributor with a two-cock section for reaction tubes. The special section is placed next to the buret (which is to the right but not shown). This arrangement serves for many types of analysis involving absorption and combustion. The five T-cocks will accommodate the slow combustion pipet and the two pairs of absorption pipets prescribed in the American Society for Testing Materials standard method for the analysis of natural gases and other fuel gases of similar type [10]. A copper-oxide tube may be connected at stopcock H. Stopcock G will accommodate any of the reaction tubes, including the triple reaction tube mentioned in the above ASTM standard for the determination of the small amounts of unsaturated hydrocarbons that may be in some natural gases or similar fuels.

It is apparent that this type of apparatus can conveniently meet the needs of both special and regular problems, and perhaps occasionally stimulate the imagination of the more enthusiastic analysts. For example, the possibility of conducting an entire analysis with dry gases has been mentioned. If this is done, it will probably be best to dry the sample en route to the buret, although water vapor in the sample may be determined volumetrically if the walls of the buret are carefully equilibrated with respect to the sample before the initial measurement of the sample. Working without water has distinct advantages. The buret remains clean, and the position of the mercury meniscus is determined with less eye strain and perhaps greater precision than is the case when films or droplets of water are on the buret walls. There is no error caused by a change in the amount of water above the mercury in the buret or by solution of any gas in the water here or in the combustion pipet. (Water formed in the combustion pipet evaporates into the dried gas passed back into

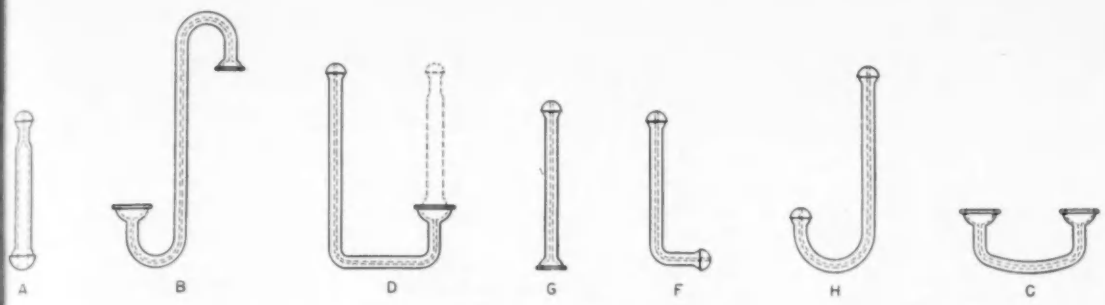

FIGURE 2. *Connectors for reaction tubes.*

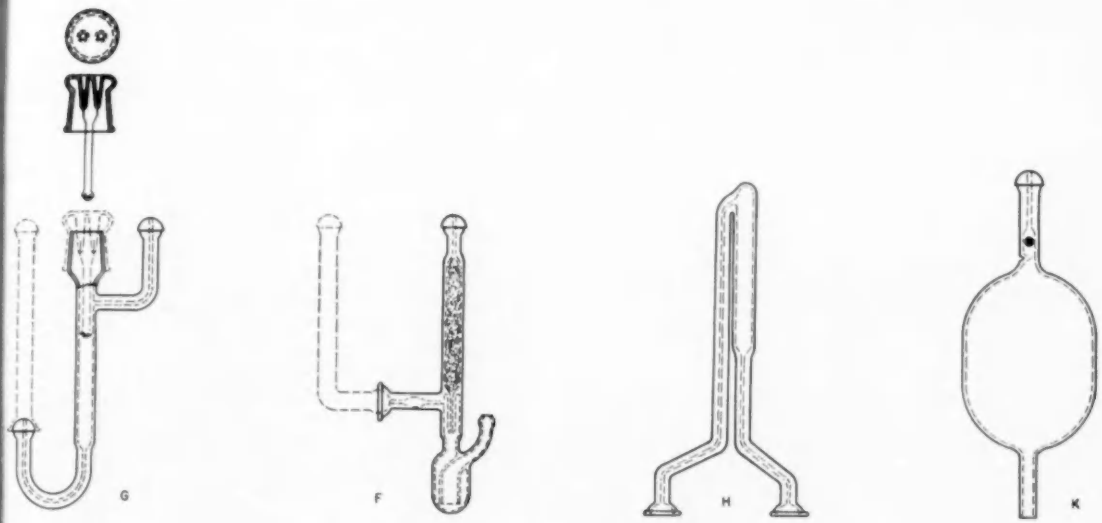

FIGURE 3. *Special reaction tubes and reservoir.*

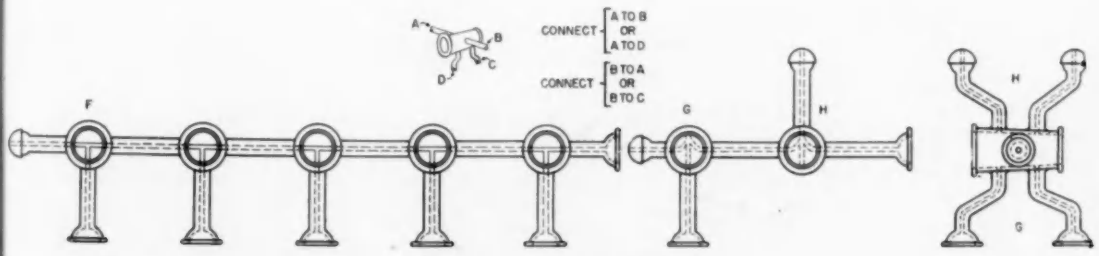

FIGURE 4. *Distributor sections.*

it during the combustion and is removed by the desiccant.) It should be noted that prolonged use of Ascarite during dry analyses may remove so much water from it that the rate of absorption of carbon dioxide on this reagent is considerably reduced. Although the likelihood of a general conversion to dry analyses is not great, every analyst should have the satisfying experience of performing a few. On the other hand, a wet analysis can be made much more dependably by interposing a saturator in the reaction tube nearest the buret, rather than the desiccant proposed for a dry analysis. One of the greatest and most frequently occurring errors in volumetric analysis is caused by failure to saturate properly each measured gas with water vapor. Samples of compressed gases, and residues returned from desiccating reagents, are often not completely saturated. The time required for saturation may be very long if water vapor must be supplied from liquid in the lower parts of the buret because the vapor travels slowly by diffusion and convection in tubes of this size.

5. References

[1] Martin Shepherd, National Geographic Society, U. S. Army Air Corps stratosphere flight of 1935 in the balloon Explorer II, Stratosphere Series No. **2,** 117 (1936).

[2] Joseph R. Branham and Martin Shepherd, J. Research NBS **22,** 171 (1939) RP1175.

[3] Martin Shepherd, J. Research NBS **26,** 351 (1941) RP1382.

[4] George Lunge and H. R. Ambler, Technical gas analysis (D. Van Nostrand Co., Inc., New York, N. Y., 1934).

[5] Martin Shepherd, J. Research NBS **38,** 19 (1947) RP1759.

[6] Martin Shepherd, BS J. Research **6,** 121 (1931) RP266.

[7] Martin Shepherd, BS J. Research **4,** 747 (1930) RP177; Joseph R. Branham and Edward C. Sperling, J. Research NBS **22,** 701 (1939) RP1214; Martin Shepherd, J. Research NBS **26,** 351 (1941) RP1382.

[8] Marthada V. Kilday, J. Research NBS **45,** 43 (1950) RP2112.

[9] Martin Shepherd, Anal. Chem. **22,** 881 (1950).

[10] Am. Soc. Testing Materials, Philadelphia, ASTM designation: D 1136–50T (1950).

Washington, July 31, 1953.

Journal of Research of the National Bureau of Standards Vol. 52, No. 1, January 1954 Research Paper 2465

Mismatch Errors in the Measurement of Ultrahigh-Frequency and Microwave Variable Attenuators

R. W. Beatty

The mismatch error in the measurement of ultrahigh-frequency and microwave variable attenuators is analyzed and expressions are derived. An example is given to show that the mismatch error in measuring the difference in attenuation between two attenuators is less than the sum of the mismatch errors obtained when measuring each attenuator individually.

1. Introduction

The error resulting from mismatched generator and detector sections in the measurement of the attenuation of a single attenuator is well known.[1] The corresponding error in the measurement of changes in attenuation is important in the calibration of variable attenuators and in the calibration of large attenuators, using known pads as gage blocks or fixed attenuation standards.

The calibration of a variable attenuator consists in measuring the change in the insertion loss as the attenuator dial moves from a zero or reference position to another position that is marked or can be read on a scale. The change in the insertion loss equals the change in attenuation if the attenuator is placed in a reflectionless, or matched, system. There is always a degree of uncertainty regarding the match, depending upon the accuracy of the instruments used to indicate or recognize matched conditions and upon the reflections from connectors. For this reason the change in the insertion loss cannot be considered to be exactly equal to the change in attenuation, and the difference is called the mismatch error.

2. Expression for Mismatch Error

A change in a variable attenuator from the reference position to another position is equivalent to removing one attenuator and inserting another attenuator in the circuit. The insertion loss, in decibels, of the attenuator [2] corresponding to the reference position of the variable attenuator is

$$L=20\log_{10}\left|\frac{(1-S_{11}\Gamma_G)(1-S_{22}\Gamma_L)-S_{12}^2\Gamma_G\Gamma_L}{S_{12}(1-\Gamma_G\Gamma_L)}\right|. \quad (1)$$

The voltage-reflection coefficients Γ_G and Γ_L refer to the generator and load, respectively, and are measured at the terminals where the attenuator is inserted. The scattering coefficients [3] S_{11}, S_{12}, and S_{22} refer to the attenuator, corresponding to the reference or zero position of the variable attenuator. The corresponding insertion loss for a different setting of the variable attenuator is

$$L'=20\log_{10}\left|\frac{(1-S'_{11}\Gamma_G)(1-S'_{22}\Gamma_L)-(S'_{12})^2\Gamma_G\Gamma_L}{S'_{12}(1-\Gamma_G\Gamma_L)}\right|. \quad (2)$$

The change in the insertion loss is

$$\Delta L=L'-L=20\log_{10}\left|\frac{1}{S'_{12}}\right|-20\log_{10}\left|\frac{1}{S_{12}}\right| +20\log_{10}\left|\frac{(1-S'_{11}\Gamma_G)(1-S'_{22}\Gamma_L)-(S'_{12})^2\Gamma_G\Gamma_L}{(1-S_{11}\Gamma_G)(1-S_{22}\Gamma_L)-S_{12}^2\Gamma_G\Gamma_L}\right|, \quad (3)$$

or

$$\Delta L=A'-A+\epsilon, \quad (4)$$

where A', A, and ϵ in eq (4) correspond to the three terms in eq (3). The error ϵ must be subtracted from the change in the insertion loss to obtain the change in attenuation, $A'-A$.

The error term can also be written [4]

$$\epsilon=20\log_{10}\left|\frac{(1-\Gamma'_1\Gamma_G)(1-S'_{22}\Gamma_L)}{(1-\Gamma_1\Gamma_G)(1-S_{22}\Gamma_L)}\right|, \quad (5)$$

where Γ_1 and Γ'_1 are the input-voltage reflection coefficients of the attenuator terminated in a load having a voltage reflection coefficient Γ_L.

The mismatch error in the measurement of a single attenuator can be obtained as a special case of eq (5). The reference attenuator vanishes in this case, changing Γ_1 to Γ_L, S_{12} to unity, and S_{11} and S_{22} to zero. Substituting these values for Γ_1 and S_{22} into eq (5) yields

$$\epsilon=20\log_{10}\left|\frac{(1-\Gamma'_1\Gamma_G)(1-S'_{22}\Gamma_L)}{1-\Gamma_G\Gamma_L}\right|, \quad (6)$$

which corresponds to eq (24), page 826 of the reference of footnote 1.

[1] C. G. Montgomery, Technique of microwave measurements, p. 824 (McGraw-Hill Book Co., Inc., New York, N. Y., 1947).

[2] See Appendix.

[3] The scattering coefficients S_{11}, S_{12}, and S_{22} are in effect defined by eq 12 and figure 2. *See also*, C. G. Montgomery, R. H. Dicke, and E. M. Purcell, Principles of microwave circuits, p. 146–151 (McGraw-Hill Book Co., Inc., New York, N. Y., 1948).

[4] Substitute $\Gamma_1=S_{11}+\frac{S_{12}^2\Gamma_L}{1-S_{22}\Gamma_L}$ and $\Gamma'_1=S'_{11}+\frac{(S'_{12})^2\Gamma_L}{1-S'_{22}\Gamma_L}$ in eq (3).

3. Evaluation of the Mismatch Errors

It is possible in principle to evaluate the mismatch error by measuring the voltage reflection coefficients Γ_G, Γ_L, Γ_1, Γ_1', S_{22}, and S_{22}', and substituting them into eq (5).

In many cases, the magnitudes of the reflection coefficients can be determined, but their phases cannot be conveniently determined because of the limitations of a particular measuring apparatus. Equation (5) can then be used to find the limits of the mismatch error, permitting the phases of the reflection coefficients to have all possible values. The limit of error can be expressed in the form

$$\epsilon_{\text{limit}} = 20 \log_{10} \frac{(1 \pm |\Gamma_1' \Gamma_G|)(1 \pm |S_{22}' \Gamma_L|)}{(1 \mp |\Gamma_1 \Gamma_G|)(1 \mp |S_{22} \Gamma_L|)}, \tag{7}$$

and the corresponding limit of error for single attenuators is

$$\epsilon_{\text{limit}} = 20 \log_{10} \frac{(1 \pm |\Gamma_1 \Gamma_G|)(1 \pm |S_{22} \Gamma_L|)}{1 \mp |\Gamma_G \Gamma_L|}. \tag{8}$$

For example, in order to reduce mismatch errors in the calibration of attenuators, the magnitudes of Γ_G and Γ_L are made as small as possible, and their probable amplitude is estimated from the accuracy of the apparatus used to recognize matched conditions and from the known connector characteristics. It is difficult to accurately determine the phases of these small reflection coefficients, and the mismatch error can generally be determined not exactly, but within limits.

An example will illustrate the determination of mismatch error. If the voltage standing-wave ratios σ_G, σ_L, σ_1, σ_1', σ_{22}, and σ_{22}' [$\sigma = (1+|\Gamma|)/(1-|\Gamma|)$] corresponding to $|\Gamma_G|$, $|\Gamma_L|$, $|\Gamma_1|$, $|\Gamma_1'|$, $|S_{22}|$, and $|S_{22}'|$ are 1.1, 1.1, 1.2, 1.5, 1.2, and 1.5, the limits of error for the initial attenuator calculated from eq (8) are approximately ± 0.095 decibel. The corresponding limits of error for the final attenuator are approximately ± 0.185 decibel. The limits of error for the change in attenuation calculated from eq (7) are approximately $\pm$ 0.242 decibel. It is seen that the mismatch error for the change in attenuation is less than the sum of the mismatch errors in measuring each attenuator individually.

It is often possible to determine the phases of Γ_1, Γ_1', S_{22}, and S_{22}', enabling one to calculate the mismatch error within narrower limits. The error in measuring voltage standing-wave ratios and phase angles produces an error in determining the limits of mismatch error but is in general a second-order effect that can be neglected.

4. Appendix. Derivation of Expression for Insertion Loss

The insertion loss of a four-terminal network is defined by the equation

$$L = 10 \log_{10} \frac{P_L}{P_2}, \tag{9}$$

where P_L denotes the power delivered directly to a load, and P_2 denotes the power delivered to that load when the network is inserted between the load and the generator. It is assumed that the generator is stable and unaffected by changes in loading.

The insertion loss of a four-terminal network can be expressed in terms of its scattering coefficients S_{11}, S_{12}, and S_{22}, and the voltage reflection coefficients Γ_G and Γ_L of the generator and the load.

Referring to figures 1 and 2, the insertion loss is

$$L = 10 \log_{10} \frac{P_L}{P_1} \cdot \frac{P_1}{P_2} = 10 \log_{10} \frac{P_L}{P_1} \cdot \frac{1}{\eta}, \tag{10}$$

where η is the efficiency of the network. If A and B denote the incident and reflected voltage waves shown in figure 2. The efficiency is [5]

$$\eta = \frac{P_2}{P_1} = \frac{E_2 \cdot (-I_2)}{E_1 \cdot I_1} = \frac{|B_2|^2 - |A_2|^2}{|A_1|^2 - |B_1|^2} = \left|\frac{B_2}{A_1}\right|^2 \frac{1-|\Gamma_L|}{1-|\Gamma_1|^2}. \tag{11}$$

The scattering equations of the network are

$$\left.\begin{aligned} B_1 &= S_{11} A_1 + S_{12} A_2 \\ B_2 &= S_{12} A_1 + S_{22} A_2 \end{aligned}\right\}, \tag{12}$$

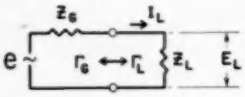

$$\Gamma_G = \frac{\bar{Z}_G - \bar{Z}_0}{\bar{Z}_G + \bar{Z}_0}; \quad \Gamma_L = \frac{\bar{Z}_L - \bar{Z}_0}{\bar{Z}_L + \bar{Z}_0}$$

$$E_L = e \frac{\bar{Z}_L}{\bar{Z}_G + \bar{Z}_L} = \frac{e}{2} \frac{(1-\Gamma_G)(1+\Gamma_L)}{(1-\Gamma_G\Gamma_L)}$$

$$I_L = \frac{E_L}{\bar{Z}_L} = \frac{e}{2\bar{Z}_0} \frac{(1-\Gamma_G)(1-\Gamma_L)}{(1-\Gamma_G\Gamma_L)}$$

$$P_L = E_L \cdot I_L = \frac{e^2}{4\bar{Z}_0} \left|\frac{1-\Gamma_G}{1-\Gamma_G\Gamma_L}\right|^2 \left\{1-|\Gamma_L|^2\right\}$$

FIGURE 1. *Load connected directly to generator.*

[5] Note that expressions of the form $E \cdot I$ represent the dot, or scalar, product of two vector quantities.

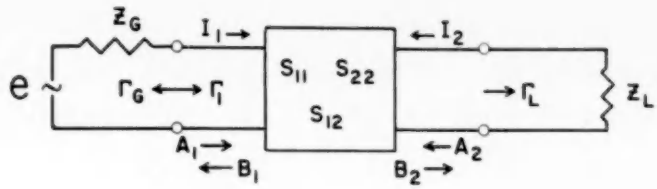

$$\begin{cases} E_1 = A_1 + B_1 \\ I_1 = \frac{1}{Z_0}(A_1 - B_1) \end{cases} \qquad \begin{cases} E_2 = A_2 + B_2 \\ I_2 = \frac{1}{Z_0}(A_2 - B_2) \end{cases} \qquad \begin{cases} \Gamma_1 = \frac{B_1}{A_1} \\ \Gamma_L = \frac{A_2}{B_2} \end{cases}$$

$$P_1 = E_1 \cdot I_1 = \frac{|A_1|^2 - |B_1|^2}{Z_0} = \frac{|A_1|^2}{Z_0}\left\{1 - |\Gamma_1|^2\right\}$$

$$P_2 = E_2 \cdot (-I_2) = \frac{|B_2|^2 - |A_2|^2}{Z_0} = \frac{|B_2|^2}{Z_0}\left\{1 - |\Gamma_L|^2\right\}$$

FIGURE 2. *Network inserted between generator and load.*

where $\Gamma_{1=B_1/A_1}$ and $\Gamma_{L=A_2/B_2}$. But

$$\frac{B_2}{A_1} = \frac{S_{12}}{1 - S_{22}\Gamma_L}, \tag{13}$$

therefore,

$$\eta = \left|\frac{S_{12}}{1 - S_{22}\Gamma_L}\right|^2 \frac{1 - |\Gamma_L|^2}{1 - |\Gamma_1|^2}. \tag{14}$$

Inspection of figure 1 leads to the conclusion

$$\frac{P_L}{P_i} = \left|\frac{1 - \Gamma_G\Gamma_1}{1 - \Gamma_G\Gamma_L}\right|^2 \cdot \frac{1 - |\Gamma_L|^2}{1 - |\Gamma_1|^2}. \tag{15}$$

Substitution of these equations into eq (8) yields

$$L = 20 \log_{10} \frac{(1 - \Gamma_G\Gamma_1)(1 - S_{22}\Gamma_L)}{S_{12}(1 - \Gamma_G\Gamma_L)}. \tag{16}$$

Since

$$\Gamma_1 = S_{11} + \frac{S_{12}^2\Gamma_L}{1 - S_{22}\Gamma_L}, \tag{17}$$

the insertion loss may also be written

$$L = 20 \log_{10} \left|\frac{(1 - S_{11}\Gamma_G)(1 - S_{22}\Gamma_L) - S_{12}^2\Gamma_G\Gamma_L}{S_{12}(1 - \Gamma_G\Gamma_L)}\right|. \tag{18}$$

WASHINGTON, August 28, 1953.

282952—54——2

Journal of Research of the National Bureau of Standards Vol. 52, No. 1, January 1954 Research Paper 2466

Heat Capacity, Heats of Transitions, Fusion, and Vaporization, and Vapor Pressure of Octafluorocyclobutane[1]

George T. Furukawa, Robert E. McCoskey, and Martin L. Reilly

The heat capacity of octafluorocyclobutane of 99.98$_5$-mole-percent purity was determined in an adiabatic calorimeter from 17° to 270° K. The heat of fusion is 2768.2 ±2.0 abs j mole^{-1} at the triple-point temperature of 232.96 ±0.05° K. The three heat-of-vaporization experiments at the vapor pressure of 590.9 mm Hg and 261.25° K gave an average value of 23721 ±20 abs j mole^{-1}. Four solid-solid transitions were observed with the heat-capacity peaks at 141.3 ±0.2°, 174.6 ±0.2°, 214.84 ±0.05°, and 216.99 ±0.05° K. The anomalous behavior in the heat capacity at about 97° K, where the heat capacity changes its slope abruptly, is attributed to glass transformation. The vapor pressure was measured from 177° to 274° K. The results of this measurement from the triple-point temperature to 274° K can be represented within ±0.5 mm Hg in most cases by the equation

$$\log_{10}p(\text{mm Hg}) = 6.70267 - \frac{1315.906}{T} + 8.778482\times10^{-3}T - 1.739691\times10^{-5}T^2.$$

The entropy of octafluorocyclobutane in the ideal gas state at 261.25° K and 1 atm was computed from the experimental data to be 380.52 ±0.71 abs j deg^{-1} mole^{-1} or 90.95 ±0.17 cal deg^{-1} mole^{-1} (1 cal=4.1840 abs j). The entropy computed from the spectroscopic assignments by Claassen and the molecular constants based on the D_{4h} model amounted to 87.83 cal deg^{-1} mole^{-1}.

1. Introduction

Octafluorocyclobutane can be prepared by pyrolysis of polytetrafluoroethylene [2] and by cyclic dimerization of tetrafluoroethylene.[3] The latter material has come into importance in the recent years as the monomer in the production of polytetrafluoroethylene plastic (Teflon), which has a remarkably high chemical and thermal stability. In order to obtain a wider thermodynamic knowledge regarding the fluorocarbons, fluorocarbon polymers, and monomers or prototype molecules, calorimetric and vapor-pressure measurements have been made with octafluorocyclobutane. This material is interesting also from the viewpoint of its structure; some [4,5] of the investigators have interpreted its vibrational spectra in terms of a planar ring model (D_{4h}). More recent spectral [6] and electron diffraction [7] studies seem to favor the nonplanar ring structure (V_d). There is at present an investigation being conducted at the Bureau to make spectral assignments in light of the evidence for a V_d structure.

Calorimetric studies with the tetrafluoroethylene [8] and the polytetrafluoroethylene [9] have been reported recently by the National Bureau of Standards.

2. Apparatus and Method

The heat-capacity, the heat-of-fusion, and the vapor-pressure measurements with the octafluorocyclobutane were carried out in the adiabatic calorimeter described previously by R. B. Scott, et al.[10] For the vapor-pressure measurements the calorimeter valve was opened to a mercury manometer, which was read by means of a mirror-backed glass scale. The calorimeter served as a thermostated container. No provision was made to stir the sample. The pressure readings were converted to standard mm Hg (g=980.665 cm sec^{-2}, temperature=0° C.) on the basis that the local gravity is 980.076 cm sec^{-2}.

The heat-of-vaporization measurements were made in another adiabatic calorimeter similar in design to those described by Osborne and Ginnings [11] and by Aston, et al.[12] This calorimeter contained a throttle valve within the space enclosed by the adiabatic shield. During the vaporization experiments, the vapor was removed isothermally by controlling the valve and introducing a known electric energy continuously. A nickel resistance thermometer wound on the tube between the valve and the calorimeter container served to sense the temperature of the vapor removed. When a desired quantity of the material was collected, the electric power was cut off and the valve closed. The heat of vaporization per mole, L, was computed from the total energy

[1] This paper is based on research sponsored by the Ordnance Corps, U. S. Department of the Army.
[2] United States Patent 2384821.
[3] United States Patent 2404374.
[4] W. F. Edgell, J. Am. Chem. Soc. **69**, 660 (1947).
[5] H. H. Claassen, J. Chem. Phys. **18**, 543 (1950).
[6] W. F. Edgell and D. G. Weiblen, J. Chem. Phys. **18**, 571 (1950).
[7] H. P. Lemaire and R. L. Livingston, J. Chem. Phys. **18**, 569 (1950).
[8] G. T. Furukawa, R. E. McCoskey, and M. L. Reilly, J. Research NBS, **51**, (1953) RP2432.
[9] G. T. Furukawa, R. E. McCoskey, and G. J. King, J. Research NBS **49**, 273 (1952) RP2364.
[10] R. B. Scott, C. H. Meyers, R. D. Rands, Jr., F. G. Brickwedde, and N. Bekkedahl, J. Research NBS **35**, 39 (1945) RP1661.
[11] N. S. Osborne and D. C. Ginnings, J. Research NBS **39**, 453 (1947) RP1841.
[12] J. G. Aston, H. L. Fink, G. J. Janz, and K. E. Russell, J. Am. Chem. Soc. **73**, 1939 (1951).

nput, Q, and the mass, m, of material collected by the relation

$$L=\frac{MQ}{m}\left(1-\frac{u}{u'}\right), \quad (1)$$

in which u and u' are the specific volumes of the liquid and vapor, respectively, at the vaporization temperature and M is the molecular weight.

All temperature measurements are in accordance with the International Temperature Scale [13] and below 90° K in accordance with a provisional scale [14] based on a set of platinum resistance thermometers calibrated against a helium-gas thermometer.

3. Material

The octafluorocyclobutane used in this investigation was kindly furnished by the E. I. du Pont de Nemours & Co. Although the sample was considered quite pure, the possible impurities were tetrafluoroethylene (C_2F_4) and chlorodifluoromethane ($CHClF_2$). The material was purified further by fractional crystallization. The procedure was similar to that described by Schwab and Wichers.[15] The purity of the material so treated was determined prior to the heat-capacity experiments from the equilibrium melting temperatures [16] and was found to be 99.98$_9$ mole percent. The equilibrium temperatures and the corresponding reciprocal of the fraction melted, F, are given in table 1. The triple-point temperature (obtained by extrapolating the temperature versus $1/F$ plot to $1/F=0$) was found to be 232.96 ± 0.05° K. (In this paper, unless defined otherwise, the figure following the plus or minus is the authors' best estimate of the uncertainty.) A second purity measurement at the end of the heat-capacity studies gave essentially the same result.

TABLE 1. *Equilibrium melting temperatures of octafluorocyclobutane*

Mole fraction impurity = 0.00613 Δ T, °K = 273.16 + °C

Reciprocal of fraction melted, $1/F$	T
	°K
12.74	[a] 232.7587
8.33	232.8012
6.74	232.8215
3.93	232.8676
2.65	232.9114
1.55	232.9278
1.22	232.9420
0.00	[b] 232.9580
Triple-point temperature, 232.96±0.05° K. Purity, 99.98$_6$ mole percent.	

[a] The temperatures given are accurate to ±0.01° K. Wherever temperatures are given to the fourth decimal, the last two figures are significant only insofar as small temperature differences are concerned.
[b] Extrapolated.

In these purity determinations the system was assumed to behave ideally and to form no solid solution.

4. Heat Capacity

The heat-capacity measurements were carried out from 17° to 270° K. The observed values are given in table 2 and are also plotted in figure 1 to show the four solid-solid transitions observed. The temperatures given in the table are the mean temperatures of heating intervals. The temperature rise associated with each heating interval is also given. The corresponding heat-capacity values, which are under conditions of saturation have been corrected for curvature (see footnote 16) and vapor saturation [17] wherever applicable.

The heat capacity in the temperature range of each transition was carefully investigated. Of the four solid-solid transitions, two were found very close together, similar to those in hydrogen bromide.[18] Equilibrium was attained within these two transitions (214.84° and 216.99° K) in the usual time of 6 to 10 min. On the other hand, the relaxation time for the transitions at the two lower temperatures (141.3° and 174.6° K) was found to be extremely long; small but definite temperature drifts were observed even 2 hr after the end of heating. On account of this long relaxation time, the heat capacity in these transition ranges was dependent somewhat upon the thermal history or the rate of cooling prior to the experiments. Thus, the results in the transition region are scattered, up to as much as 0.3 percent. The peaks of the heat capacities within the four transitions were found to be 141.3 ± 0.2°, 174.6 ± 0.2°, 214.84 ± 0.05°, and 216.99 ± 0.05° K. The heat of transition was not determined for any given temperature; instead, the enthalpy change was determined for an interval of convenient temperatures, which included the transition. These results are given in section 5.

Figure 1 shows an anomalous behavior in the region of 97° K, in which the heat capacity under goes a rather abrupt change in slope. Also, a longer time (about 30 min) was required for temperature equilibrium. A magnified plot of this temperature range is shown in figure 2. The cooling rate prior to the heat-capacity measurements had a decided effect upon the results in this temperature range. Slow cooling yielded significantly higher values. As pointed out in section 5, the increase in the enthalpy change corresponding to the higher heat-capacity values in this temperature range seems to be offset by an almost equal enthalpy change decrease in the interval 130° to 150° K.

Although not as pronounced, the heat-capacity behavior of the substance near 97° K is similar to the glass transformation found in organic glasses,[19] high polymers,[20] and other noncrystalline solids. Similar

[13] H. F. Stimson, J. Research NBS **42**, 209 (1949) RP1962.
[14] H. J. Hoge and F. G. Brickwedde, J. Research NBS **22**, 351 (1939) RP1188.
[15] F. W. Schwab and E. Wichers, J. Research NBS **32**, 253 (1944) RP588.
[16] G. T. Furukawa, D. C. Ginnings, R. E. McCoskey, and R. A. Nelson, J. Research NBS **46**, 195 (1951) RP2191.
[17] H. J. Hoge, J. Research NBS **36**, 111 (1946) RP1693.
[18] W. F. Giauque and R. W. Wiebe, J. Am. Chem. Soc. **50**, 2193 (1928).
[19] G. S. Parks, H. M. Huffman, and F. R. Cattoir, J. Phys. Chem. **32**, 1366 (1928).
[20] G. T. Furukawa, R. E. McCoskey, and G. J. King, J. Research NBS **50**, 357 (1953) RP2425.

TABLE 2. *Observed molal heat capacities of octafluorocyclobutane*

Molecular weight=200.04; °K=273.16 +°C

T	$C_{satd.}$	ΔT
	RUN 1	
°K	abs j deg^{-1} mole^{-1}	°K
221.27	188.13	4.0158
225.27	190.01	3.9845
229.23	191.99	3.9511
	Fusion	
234.73	199.00	3.1500
237.87	199.87	3.1335
241.00	200.70	3.1194
246.04	202.28	6.9656
253.35	204.48	7.6644
260.98	207.05	7.5822
268.52	209.77	7.5034
	RUN 2	
210.25	191.77	1.6640
211.95	195.46	1.7359
213.80	252.55	1.9638
	Transition	
215.78	273.48	1.8586
	Transition	
219.71	187.58	2.3583
222.06	188.58	2.3493
226.60	190.70	2.3288
229.82	192.53	4.1002
	RUN 3	
126.76	125.18	9.1535
134.47	143.70	6.2668
138.99	174.84	2.7702
	Transition	
144.24	157.16	3.9023
148.23	143.83	4.0824
154.30	145.00	8.0648
	RUN 4	
111.38	105.60	6.6270
118.42	113.37	7.4492
126.77	124.99	9.2458
135.03	147.21	7.2735
139.90	210.26	2.4853
	Transition	
142.02	264.30	1.0615
143.26	169.51	1.4173
144.98	151.79	2.0136
147.02	145.33	2.0588
149.08	143.23	2.0686
151.15	142.75	2.0665
157.23	146.69	10.1044
171.49	159.08	0.9510
172.52	160.67	1.1034
173.50	189.08	0.8580
	RUN 5	
163.21	151.63	9.8138
169.55	157.59	2.8631
172.12	159.45	2.3639
173.77	210.46	0.9319
	Transition	
175.84	154.63	.9589
176.71	155.28	.7965
178.06	156.72	1.8992
179.96	158.21	1.8869
185.59	162.94	9.3856
194.74	171.42	8.9116

T	$C_{satd.}$	ΔT
	RUN 6	
°K	abs j deg^{-1} mole^{-1}	°K
181.58	159.24	7.3718
189.74	166.45	8.9346
198.52	175.39	8.6249
205.40	184.12	5.1513
208.87	189.66	1.7764
210.70	193.13	1.8886
211.43	193.57	1.6146
212.83	199.60	1.1887
213.82	202.47	0.7842
	Transition	
216.32	215.00	$_{v}$.5659
	Transition	
	RUN 7	
55.86	57.77	5.8959
61.45	62.25	5.2849
66.52	66.36	4.8475
71.20	69.94	4.5216
75.59	73.45	4.2568
80.13	77.26	4.8230
84.83	81.22	4.5657
89.29	84.90	4.3577
93.57	87.92	4.1982
98.17	91.30	5.0130
103.07	96.60	4.7848
	RUN 8	
18.13	17.18	0.1117
18.56	18.14	.7424
19.49	19.80	1.1328
21.69	23.59	3.2563
24.64	28.17	2.6484
27.11	31.60	2.2921
29.92	35.06	3.3206
32.89	38.40	2.6231
36.49	41.97	4.5760
40.89	46.00	4.2323
46.20	50.27	6.3786
52.43	55.34	6.0745
58.16	59.72	5.3968
63.31	63.86	4.8957
	RUN 9	
17.45	16.21	1.4819
18.83	18.69	1.2747
20.03	20.84	1.1343
21.24	22.87	1.2789
22.57	24.96	1.3893
	RUN 10	
82.20	79.04	5.7036
86.41	82.66	2.7175
89.09	84.79	2.6443
91.71	86.69	2.5828
	RUN 11	
93.29	87.49	2.9379
95.99	89.05	2.4637
98.43	90.72	2.4207
100.82	94.44	2.3531
103.53	97.38	3.0604

T	$C_{satd.}$	ΔT
	RUN 12	
°K	abs j deg^{-1} mole^{-1}	°K
92.25	87.06	2.5503
94.77	88.50	2.5009
97.25	90.29	2.4518
99.67	93.09	2.3915
95.49	89.18	2.5237
	RUN 13	
228.41	191.64	1.9694
229.92	192.72	1.0469
	Fusion	
237.23	200.02	4.7629
241.97	201.47	4.7318
	RUN 14	
86.06	82.37	2.5249
88.62	84.46	2.6105
91.13	86.26	2.4014
93.89	88.03	3.1275
96.61	89.48	2.2982
99.25	92.32	2.9847
101.83	95.50	2.1792
104.34	98.17	2.8383
107.14	103.97	2.7717
	RUN 15	
87.34	83.47	2.1532
89.65	85.24	2.4628
92.09	87.05	2.4078
94.47	88.86	2.3574
96.80	90.86	2.3098
99.09	93.14	2.2602
101.69	96.06	2.9378
104.65	98.98	2.9830
	RUN 16	
82.82	79.59	2.7401
85.95	82.23	3.5220
89.41	85.06	3.3966
92.76	87.58	3.2829
96.00	90.14	3.1997
99.16	93.18	3.1057
102.22	96.70	3.0126
106.89	101.06	2.8944
110.69	104.94	4.7038
115.31	109.68	4.5350
120.30	115.56	5.4474
126.13	123.93	6.2149
	Transition	
133.42	144.17	3.6295

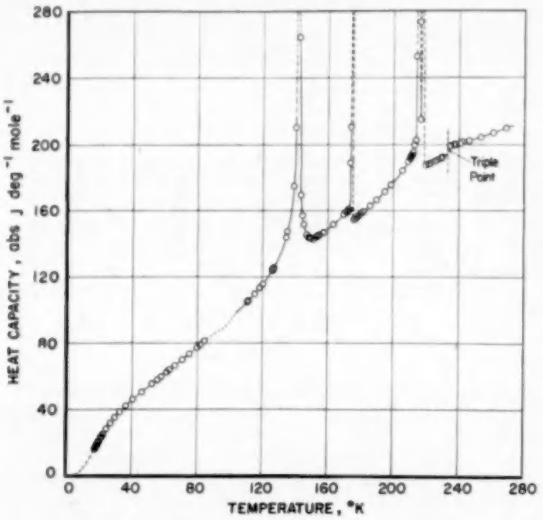

FIGURE 1. *Observed heat capacities of octafluorocyclobutane.*

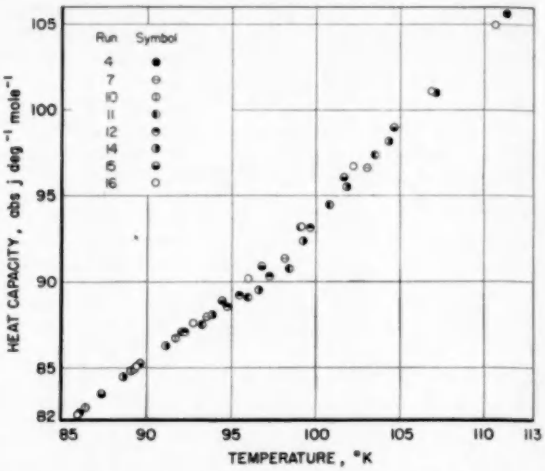

FIGURE 2. *Observed heat capacities of octafluorocyclobutane from 85° to 113° K.*

behavior was reported by Huffman, et al.[21] for cyclopentene and other compounds.

The heat-capacity values given in table 2 are probably accurate to 0.2 percent, except in the transition regions of 141.3° and 174.6° K, the anomalous region of 97° K, and the temperature range below 50° K, where larger tolerances must be allowed.

5. Heats of Fusion and Transitions

The heat of fusion was determined in the usual manner by introducing a known electric energy from a temperature just below the triple point to just above it and correcting for the premelting and heat capacity. The results of three measurements are summarized in table 3. The values given in the fourth column are the total heats required to melt 141.9302 g of the sample in the calorimeter. Considering the precision of the measurements and various sources of error, the uncertainty of the heat of fusion is believed to be ± 2.0 abs j mole^{-1}.

TABLE 3. *Molal heat of fusion of octafluorocyclobutane*

Molecular weight—200.04; mass of sample—141.9302 g; triple-point temperature = 232.95° K; °K = 273.16 + °C

Temperature interval	Heat input	Heat capacity and premelting correction	ΔH	ΔH_f
°K	*abs j*	*abs j*	*abs j*	*abs j mole*$^{-1}$
227.6435 to 237.3363	4199.9	2236.9	1963.0	2766.7
227.7655 to 234.7512	3567.3	1602.2	1965.1	2769.8
227.4253 to 234.8109	3657.7	1693.9	1963.8	2768.0
Mean heat of fusion				2768.2
Standard deviation				±0.7

[21] H. M. Huffman, M. Eaton, and G. D. Oliver, J. Am. Chem. Soc. **72**, 2911 (1948).

TABLE 4. *Molal enthalpy changes over even temperature intervals, including the solid-solid transitions and the anomalous region*

Molecular weight = 200.04; °K = 273.16 + °C

Temperature interval	Total energy input	Heat capacity correction	ΔH
		$H_{151°\,K} - H_{150°\,K}$	
°K	*abs j mole*$^{-1}$	*abs j mole*$^{-1}$	*abs j mole*$^{-1}$
122.1832 to 150.2725 [a]	5095.7	−1010.0	4085.7
133.2603 to 150.6635 [b]	3739.7	+346.0	4085.7
		Mean	4085.7
129.2400 to 151.6058 [b] [c]	4405.2	−328.8	4076.4
		$H_{180°\,K} - H_{170°\,K}$	
170.9367 to 180.8963 [a]	5002.3	+6.0	5008.3
168.7525 to 177.2341 [b]	4768.1	+237.8	5005.9
		Mean	5007.1
		$H_{220°\,K} - H_{210°\,K}$	
209.4137 to 220.8877 [a]	4878.4	−278.9	4599.5
212.4227 to 222.1278 [b]	4529.9	+70.0	4599.9
		Mean	4599.7
		$H_{105°\,K} - H_{90°\,K}$	
87.1084 to 105.4621 [a]	1659.0	−289.9	1369.1
89.9824 to 105.7577 [a]	1450.4	−81.2	1369.2
		Mean	1369.2
88.4184 to 106.1372 [a] [c]	1626.9	−247.7	1379.2
87.7140 to 103.7215 [a] [c]	1446.5	−67.3	1379.2
		Mean	1379.2

[a] Heated in increments over this temperature interval under adiabatic conditions.

[b] Heated continuously over this temperature interval under adiabatic conditions.

[c] The sample was cooled slowly over 1 week from 230° to 80° K prior to the heat-capacity measurements.

As mentioned in section 4, in the temperature range of the four solid-solid transitions, small increments of heat were added to obtain the shape of the heat-capacity curve. Instead of attempting to determine the heat of transition at a given temperature, the enthalpy change was determined over an interval of convenient temperatures. This was done both by summing the increments of heats added in the determination of the shape of the heat-capacity curve and by heating continuously through this interval. The results of both experimental methods are summarized in table 4. The values given in the third column are corrections used to reduce the enthalpy changes to the even temperature intervals indicated. The anomalous region was treated in a similar manner by summing the heats added in the interval from 90° to 105° K. In one series of measurements (see table 2, runs 15 and 16), the material was cooled slowly over a period of 1 week from 230° to 80° K. The enthalpy change, as well as the heat capacity in the interval 90° to 105° K, was higher. The enthalpy change from 90° to 105° K was 10.0 abs j mole^{-1} higher. Also, there was found a decrease in the enthalpy change in the interval 130° to 150° K of 9.3 abs j mole^{-1}.

6. Heat of Vaporization

Three heat of vaporization experiments were made at 261.25° K (p=590.9 mm Hg). The experimentally observed quantity, MQ/m, the conversion factor, $1-u/u'$, and the heat of vaporization, L, are given in table 5. The specific volumes, u and u', for this material were kindly furnished by the E. I. du Pont de Nemours & Co. Considering the precision obtained and various sources of error, the uncertainty of the heat-of-vaporization value is believed to be ±20 abs j mole^{-1}.

TABLE 5. *Molal heat of vaporization of octafluorocyclobutane at 261.25° K*

Pressure=590.9 mm Hg; molecular weight=200.04; °K=273.16+°C

MQ/m	$1-u/u'$	L
abs j mole^{-1}		*abs j mole*$^{-1}$
23,842	0.99550	23,735
23,823	.99550	23,716
23,818	.99550	23,711
Mean		23,721
Standard deviation		±6

7. Vapor Pressure

As there was no provision made to stir the sample, several series of vapor-pressure measurements were made under different conditions to make certain that temperature equilibrium was attained. The measurements were made going down the temperature scale as well as up. The close agreement in the results given in table 6 indicates that good temperature equilibrium existed. The results above the triple-point temperature (232.96° K) were fitted to an equation given by

$$\log_{10} p(\text{mm Hg}) = 6.70267 - \frac{1315.906}{T} + 8.778482\times10^{-3}T - 1.739691\times10^{-5}T^2.$$

The observations are compared with this equation in table 6. The equation gives the normal boiling temperature as 267.17±0.01° K and the triple-point pressure as 142.8 ±0.3 mm Hg.

TABLE 6. *Vapor pressure of octafluorocyclobutane*

° K=273.16+° C

$T_{obs.}$	$p_{obs.}$	$p_{calc.}$	$p_{obs.}-p_{calc.}$	$T_{obs.}$	$p_{obs.}$	$p_{calc.}$	$p_{obs.}-p_{calc.}$
Series I				°K	*mm* Hg	*mm* Hg	*mm* Hg
				241.32	226.3	226.5	−.2
°K	*mm* Hg	*mm* Hg	*mm* Hg	246.99	303.3	303.3	.0
267.89	782.6	782.9	−0.3	253.01	406.5	406.5	.0
270.95	886.2	885.9	.3	259.51	547.3	547.6	−.3
273.63	984.8	984.2	.6	263.88	661.9	662.2	−.3
				266.65	743.7	743.9	−.2
Series II				Series III			
179.16	5.0	....	.....	177.36	4.9	....	.....
191.94	8.2	....	.....	191.82	8.2	....	.....
201.23	14.7	....	.....	196.86	10.9	....	.....
215.30	43.4	....	.....	197.17	11.0	....	.....
223.60	77.7	....	.....	206.70	21.7	....	.....
230.81	125.7	....	.....	213.09	35.9	....	.....
232.91	142.4	142.5	−0.1	221.60	67.7	....	.....
233.16	144.6	144.5	.1	271.94	921.4	921.3	0.1

8. Experimental Entropy

The experimental data were used to calculate the entropy of the octafluorocyclobutane in the ideal gas state at 261.25° K and 1 atm. The results of the various calculations are summarized in table 7. In the temperature intervals in which the transitions occurred, the entropy change was evaluated by summing the various experimentally observed $C\Delta T/T$'s, where C is the observed heat capacity, ΔT the temperature rise, and T the midtemperature of the heating interval. The entropy change so obtained was corrected to the even temperatures indicated in table 7. Below 180° K, the results from the slow-cooling experiments were used to evaluate the en-

TABLE 7. *Summary of the experimental molal entropy of octafluorocyclobutane*

Molecular weight=200.04; °K=273.16+°C

	abs j deg^{-1} *mole*$^{-1}$
$S_{15°}$, Debye	4.38±0.04
$\Delta S_{15°-90°}$, numerical	78.24±0.16
$\Delta S_{90°-105°}$, transition	14.15±0.10
$\Delta S_{105°-130°}$, numerical	24.03±0.05
$\Delta S_{130°-150°}$, transition	29.14±0.06
$\Delta S_{150°-170°}$, numerical	18.67±0.04
$\Delta S_{170°-180°}$, transition	28.65±0.03
$\Delta S_{180°-210°}$, numerical	26.54±0.05
$\Delta S_{210°-220°}$, transition	21.32±0.02
$\Delta S_{220°-232.96°}$, numerical	10.92±0.02
$\Delta S_{232.96°}$, fusion, 2768.2/232.96	11.88±0.01
$\Delta S_{232.96°-261.25°}$, numerical	23.22±0.04
$\Delta S_{261.25°}$, vaporization, 23721/261.25	90.80±0.09
$\Delta S_{261.25°}$, gas imperfection	0.67
$\Delta S_{261.25°}$, compression	−2.09
Entropy, ideal gas at 261.25° K and 1 atm	380.52±0.71

tropy. The gas-imperfection correction was computed on the assumption that the octafluorocyclobutane vapor can be represented by the Berthelot equation of state. The critical constants used were those reported by Renfrew and Lewis.[22]

The uncertainties given in table 7 were based on the precision, the probable nonreproducibility of the physical state below 180° K, and various other sources of error. The absolute entropy obtained is probably in error by more than is given in the table because the results of the measurements indicate a certain degree of glassy state or randomness in the solid at the lower extreme of our measurements.

9. Entropy From Molecular and Spectroscopic Data

The entropy of the gaseous octafluorocyclobutane was computed from the molecular and spectroscopic data based on the D_{4h} structure. The results are summarized and compared with the calorimetric entropy in table 8. The rotational entropy was computed directly from the principal moments of inertia given by Smith, et al.[23] in which the C—C and C—F bond distances and C—C—C and F—C—F angles were 1.53 A and 1.36 A and 90 deg. and 112 deg., respectively. The moments of inertia were $I_x=I_y=796\times10^{-40}$ g-cm² and $I_z=951\times10^{-40}$ g-cm². The vibrational entropy was calculated on the basis of the assignments by Classen (see footnote 5).

On the basis of the existence of residual entropy in the calorimetric work, the discrepancy in the two results given in table 8 would be increased. Work is now in progress at the Bureau on the reassignment of the frequencies on the basis of the recent evidence for a V_d structure.

TABLE 8. *Molal entropy of octafluorocyclobutane at 261.25° K from molecular and spectroscopic data*

Molecular weight=200.04; °K=273.16+°C; 1 cal=4.1840 abs ...

	cal deg⁻¹ mole⁻¹
S, translation	41.13
S, rotation	25.65
S, vibration	21.05
S, total, ideal gas at 261.25° K and 1 atm	87.83
S, calorimetric	90.95

The authors are indebted to E. I. Du Pont de Nemours & Co. for the sample of purified octafluorocyclobutane.

WASHINGTON, July 24, 1953.

[22] M. M. Renfrew and E. E. Lewis, Ind. Eng. Chem. **38**, 870 (1946).
[23] D. C. Smith, J. R. Nielsen, L. H. Berryman, H. H. Claassen, and R. L. Hudson, NRL Report 3567 (September 15, 1949).

Journal of Research of the National Bureau of Standards Vol. 52, No. 1, January 1954 Research Paper 2467

A Characterization of Normal Matrices[1]

Alan J. Hoffman and Olga Taussky

A matrix A is called normal if $AA^*=A^*A$, where A^* is the transposed and conjugate matrix of A. It is known that for a pair of commuting matrices, A, B, there exists an ordering of the characteristic roots $\alpha_1, \ldots, \alpha_n$ of A and $\beta_1, \ldots, \beta_n$ of B, such that every polynomial $p(A,B)$ has as characteristic roots the numbers $p(\alpha_i,\beta_i)$. This property is, in general, weaker than commutativity, but does imply it if $B=A^*$. It is shown that this property already implies commutativity of A and A^* if it is assumed to hold for only one polynomial, provided the latter is suitably chosen. Polynomials of first and second degree are examined for their suitability.

Normal matrices can be characterized in many ways. In the original definition [1][2] a matrix A is called normal if $AA^*=A^*A$, where A^* is the transposed and conjugate matrix of A. It is known that for a pair of commuting matrices A, B, there exists an ordering of the characteristic roots $\alpha_1, \ldots, \alpha_n$ of A and $\beta_1, \ldots, \beta_n$ of B, such that every polynomial $p(A,B,)$ has as characteristic roots the numbers $p(\alpha_i,\beta_i)$, see [2]. This property is, in general, weaker than commutativity, but does imply it if $B=A^*$. This follows from the fact that two matrices with this property can be transformed to upper triangular form simultaneously by a unitary similarity transformation [3]. Even if the property is assumed only for linear polynomials $p(A,A^*)$, commutativity follows. This is a consequence of the fact that A is the sum of two normal matrices,

$$A=\frac{A+A^*}{2}+\frac{A-A^*}{2}.$$

For the matrices $(A+A^*)/2$, $(A-A^*)/2$ will again have the above property with respect to linear polynomials; this, however, implies that they commute [4, 5]. Hence A and A^* commute.

It will now be shown that the above property already implies the commutativity of A and A^* if it is assumed to hold for only one polynomial, provided the latter is suitably chosen. Two special results in this direction were obtained earlier [6]; the polynomials considered then were $A+A^*$ and AA^*, and it was assumed that the special ordering of the characteristic roots implied that $\beta_i=\bar{\alpha}_i$.

Certain polynomials of first and second degree are examined for their suitability. The result is that any polynomial of first degree is suitable, while not every polynomial of second degree is, although a large class among them is suitable.

In what follows we assume that $A=(a_{ik})$ is an $n\times n$ matrix with complex numbers as elements.

THEOREM 1. *If $\alpha_1, \ldots, \alpha_n$ are the eigenvalues of an $n\times n$ matrix A, α and β are two complex numbers different from 0, and the eigenvalues of $\alpha A+\beta A^*$ are $\alpha\alpha_i+\beta\bar{\alpha}_{P_i}$, where P is a permutation of the integers $1, \ldots, n$, then A is normal.*

PROOF. It is clearly no restriction to assume $\beta=1$. Further, since the hypothesis and conclusion of the theorem are concerned with eigenvalues of an operator A in unitary n-space, we may assume that an orthonormal basis has been chosen in the unitary n-space, so that the matrix A is (upper) triangular; i. e., $a_{ik}=0$ for $i>k$, and $a_{ii}=\alpha_i$. We shall show that

$$a_{ik}=0 \qquad \text{for } i\neq k, \tag{1}$$

which implies that A is normal.

The argument is based on the fact that the second elementary symmetric function S_2 of the eigenvalues $\gamma_1, \ldots, \gamma_n$ of $\alpha A+A^*$ may be computed in two ways. First, since

$$\gamma_i=\alpha\alpha_i+\bar{\alpha}_{P_i} \qquad (i=1, \ldots, n),$$

we have

$$2S_2=\sum_{i=1}^{n}\sum_{k\neq i}[\alpha^2\alpha_i\alpha_k+\bar{\alpha}_{P_i}\bar{\alpha}_{P_k}+\alpha(\alpha_i\bar{\alpha}_{P_k}+\bar{\alpha}_{P_i}\alpha_k)]. \tag{2}$$

Second, since S_2 is also the sum of all principal 2×2 minors M_{ik} of $\alpha A+A^*$, we have

$$2S_2=\sum_{i=1}^{n}\sum_{k\neq i}M_{ik}=\sum_{i=1}^{n}\sum_{k\neq i}[\alpha^2\alpha_i\alpha_k+\bar{\alpha}_i\bar{\alpha}_k + \alpha(\alpha_i\bar{\alpha}_k+\bar{\alpha}_i\alpha_k-a_{ik}\bar{a}_{ik})]. \tag{3}$$

As i and k range over all possible distinct ordered pairs of elements of the set $\{1, \ldots, n\}$, so do P_i and P_k. Hence if we subtract (3) from (2), we obtain

$$\sum_{i=1}^{n}\sum_{k\neq i}(\alpha_i\bar{\alpha}_{P_k}+\bar{\alpha}_{P_i}\alpha_k-\alpha_i\bar{\alpha}_k-\bar{\alpha}_i\alpha_k+a_{ik}\bar{a}_{ik})=0. \tag{4}$$

But $a_{ik}\bar{a}_{ik}\geq 0$. Therefore, if we show that

$$R\sum_{i=1}^{n}\sum_{k\neq i}(\alpha_i\bar{\alpha}_{P_k}+\bar{\alpha}_{P_i}\alpha_k-\alpha_i\bar{\alpha}_k-\bar{\alpha}_i\alpha_k)\geqq 0, \tag{5}$$

then (4) will imply (1).

[1] The preparation of this paper was sponsored (in part) by the Office of Scientific Research, United States Air Force.

[2] Figures in brackets indicate the literature references at the end of this paper.

Write

$$\alpha_j=\lambda_j+i\mu_j \qquad (j=1, \ldots, n),$$

where λ_j and μ_j are real.

Then (5) becomes

$$2\sum_{i=1}^{n}\sum_{k\neq i}[\lambda_i(\lambda_{Pk}-\lambda_k)+\mu_i(\mu_{Pk}-\mu_k)]\geq 0. \tag{6}$$

We shall prove

$$\sum_{i=1}^{n}\sum_{k\neq i}\lambda_i(\lambda_{Pk}-\lambda_k)\geq 0. \tag{7}$$

The same argument will apply to the μ's, and hence (6) will be established. Now for fixed i,

$$\sum_{k\neq i}\lambda_i(\lambda_{Pk}-\lambda_k)=\lambda_i\sum_{k\neq i}(\lambda_{Pk}-\lambda_k)=\lambda_i(\lambda_i-\lambda_{Pi}).$$

Hence (7) is equivalent to

$$\sum_{i=1}^{n}\lambda_i(\lambda_i-\lambda_{Pi})\geq 0. \tag{8}$$

Inequality (8) is a special case of a known inequality ([7], theorem 368), which states that if $a_1\geq \ldots \geq a_n$, $b_1\geq \ldots \geq b_n$, and P is any permutation of $\{1, \ldots, n\}$, then

$$\sum a_i b_i \geq \sum a_i b_{Pi}. \tag{9}$$

Set $a_i=b_i=\lambda_i$, and (8) is an immediate consequence of (9).

THEOREM 2.[3] *If $\alpha_1, \ldots, \alpha_n$ are the eigenvalues of an $n\times n$ matrix A, and the eigenvalues of AA^* are $\alpha_1\bar{\alpha}_{P1}, \ldots, \alpha_n\bar{\alpha}_{Pn}$, where P is a permutation of the integers $1, \ldots, n$, then A is normal.*

PROOF. As in theorem 1, we may assume A is upper triangular. We shall compute trace AA^* in two ways. First, since trace AA^* is the sum of the eigenvalues of AA^*, we have by hypothesis

$$\text{trace } AA^*=\sum_{i=1}^{n}\alpha_i\bar{\alpha}_{Pi}, \qquad \alpha_i\bar{\alpha}_{Pi}\geq 0. \tag{10}$$

Second, since trace AA^* is the sum of the elements on the diagonal of AA^*, we have

$$\text{trace } AA^*=\sum_{i=1}^{n}\alpha_i\bar{\alpha}_i+\sum_{i=1}^{n}\sum_{k\neq i}a_{ik}\bar{a}_{ik}. \tag{11}$$

Write $\alpha_j=\rho_j e^{(\theta)}{}_j$ where $\rho_j\geq 0$. We have, from (11) and (10),

$$\sum_{i=1}^{n}\rho_i^2+\sum_{i=1}^{n}\sum_{k\neq i}^{n}a_{ik}\bar{a}_{ik}=\sum_{i=1}^{n}\rho_i\rho_{Pi}. \tag{12}$$

But from inequality (8), we see that

$$\sum_{i=1}^{n}\rho_i^2\geq\sum_{i=1}^{n}\rho_i\rho_{Pi}. \tag{13}$$

[3] This theorem can also be proved from known inequalities, see [8], between the eigenvalues of a matrix A and the eigenvalues of AA^*.

Since $a_{ik}\bar{a}_{ik}\geq 0$, the only way for (12) and (13) to be consistent is for

$$a_{ik}\bar{a}_{ik}=0 \qquad \text{for all } i\neq k;$$

i. e., A is normal.

One can use essentially the same argument to establish

THEOREM 3. *Let $\alpha_1, \ldots, \alpha_n$ be the eigenvalues of an $n\times n$ matrix A, P a permutation of the integers $1, \ldots, n$, and $a_1, a_2, b_1, b_2, c_1, c_2$ complex numbers. Let the eigenvalues of*

$$a_1A+a_2A^*+b_1A^2+b_2A^{*2}+c_1AA^*+c_2A^*A \tag{14}$$

be

$$a_1\alpha_i+a_2\bar{\alpha}_{Pi}+b_1\alpha_i^2+b_2\bar{\alpha}_{Pi}^2+c_1\alpha_i\bar{\alpha}_{Pi}+c_2\bar{\alpha}_{Pi}\alpha_i \quad (i=1, \ldots, n).$$

If, in addition

$$c_1+c_2\neq 0, \tag{15}$$

then A is normal.

What if condition (15) is omitted; i. e., if $c_1=c_2$? Then theorem 3 may not hold. There are two cases to consider:

$$\text{(i) } c_1=0, \text{ (ii) } c_1\neq 0.$$

In case (i), if $b_1=b_2=0$, then the theorem reduces to theorem 1, so A is normal (unless $a_1a_2=0$, where the theorem fails). The theorem fails unless $b_1=b_2=0$. A counterexample is furnished by

$$\begin{pmatrix} c & d \\ 0 & 0 \end{pmatrix},$$

where $d\neq 0$ is arbitrary, $c=-a_1/b_1$ (if $b_1\neq 0$), or $c=-a_2/b_2$ (if $b_2\neq 0$).

For case (ii), the situation is somewhat more complicated. For example, if a_1a_2 is real and negative, the theorem fails, as one can see from the counterexample

$$\begin{pmatrix} 0 & a \\ 0 & 0 \end{pmatrix},$$

where $a^2c_1^2=-a_1a_2$.

On the other hand, if (14) is formally Hermitian, the theorem *does* hold. Specifically, we have

THEOREM 4. *Let $\alpha_1, \ldots, \alpha_n$ be the eigenvalues of an $n\times n$ matrix A; let P be a permutation of the integers $1, \ldots, n$; a, b complex numbers, c, d real numbers not both 0; let the eigenvalues of*

$$aA+\bar{a}A^*+bA^2+\bar{b}A^{*2}+cAA^*+dA^*A \ (c, d \text{ real, not both } 0) \tag{16}$$

be

$$a\alpha_i+\bar{a}\bar{\alpha}_{Pi}+b\alpha_i^2+\bar{b}\bar{\alpha}_{Pi}^2+c\alpha_i\bar{\alpha}_{Pi}+d\bar{\alpha}_{Pi}\alpha_i \quad (i=1, \ldots, n);$$

then A is normal.

PROOF. If $c \neq -d$, the situation is covered by theorem 3. If $c=-d$, it is clearly no loss of generality to take $c=1$, $d=-1$. Now order the eigenvalues of A, so that

$$R(a\alpha_1+b\alpha_1^2) \geq \ . \ . \ . \ \geq R(a\alpha_n+b\alpha_n^2). \tag{17}$$

We may assume that A is upper triangular, and that the eigenvalues of A appear on the main diagonal in the order $\alpha_1, \alpha_2, \ . \ . \ . \ , \alpha_n$.

Then let B stand for the Hermitian matrix (16), and denote its eigenvalues by $\beta_1 \geq \ . \ . \ . \ \geq \beta_n$.

It has been shown ([9], theorem I) that

$$\begin{aligned} b_{11} &\leq \beta_1 \\ b_{11}+b_{22} &\leq \beta_1+\beta_2 \\ &\ . \\ &\ . \\ &\ . \\ b_{11}+ \ . \ . \ . \ +b_{n-1,n-1} &\leq \beta_1+ \ . \ . \ . \ +\beta_{n-1}. \end{aligned} \tag{18}$$

But

$$b_{11}=2R(a\alpha_1+b\alpha_1^2)+\sum_{k=2}^{n} a_{1k}\bar{a}_{1k}, \tag{19}$$

and

$$\beta_1=\max[R(a\alpha_i+\overline{a}\alpha_{P_i}+b\alpha_i^2+\overline{b}\alpha_{P_i}^2)] \leq 2R(a\alpha_1+b\alpha_1^2), \tag{20}$$

by (17). Since $a_{1k}\bar{a}_{1k} \geq 0$ $(k=2, \ . \ . \ . \ , n)$, the only way for (19) and (20) to be consistent with the first inequality of (18) is if

$$a_{1k}=0 \qquad (k=2, \ . \ . \ . \ ,n). \tag{21}$$

Now, in view of (21), it follows that

$$b_{11}+b_{22}=2R[a(\alpha_1+\alpha_2)+b(\alpha_1^2+\alpha_2^2)]+\sum_{k=3}^{n} a_{2k}\bar{a}_{2k}, \tag{22}$$

and

$$\begin{aligned} \beta_1+\beta_2=\max_{i \neq j} R\{&a(\alpha_i+\alpha_j)+\bar{a}(\bar{\alpha}_{P_i}+\bar{\alpha}_{P_j} \\ &+b(\alpha_i^2+\alpha_j^2)+\bar{b}(\bar{\alpha}_{P_i}^2+\bar{\alpha}_{P_j}^2)\} \\ \leq 2R[&a(\alpha_1+\alpha_2)+b(\alpha_1^2+\alpha_2^2)]. \end{aligned} \tag{23}$$

The only way for (22) and (23) to be consistent with the second inequality of (18) is if $a_{2k}=0$ $(k=3, \ . \ . \ . \ ,n)$.

Continuing in this way, one sees easily that $i \neq k$ implies $a_{ik}=0$; hence, A is normal.

The authors thank J. Todd and H. Wielandt for helpful comments.

---

[1] O. Toeplitz, Der algebraische Analogon zu einen Satze von Fejér, Math. Z. **2,** 187–197 (1918).
[2] G. Frobenius, Über vertauschbare Matrizen, Sitzber. preuss. Akad. Wiss. 601–614 (1896).
[3] M. P. Drazin, J. W. Dungey, and K. W. Gruenberg, Some theorems on commutative matrices, J. London Math. Soc. **26,** 221–228 (1951)
[4] N. Wiegmann, Pairs of matrices with property L, Proc. Am. Math. Soc. **4,** 35–36 (1953).
[5] H. Wielandt, Pairs of matrices with property L, J Research NBS **51** (1953) RP2436.
[6] W. V. Parker, The characteristic roots of matrices, Duke Math. J. **12,** 519–526 (1945).
[7] G. H. Hardy, J. E. Littlewood, and G. Pólya, Inequalities, p. 261 (Cambridge Univ. Press, 1934).
[8] H. Weyl, Inequalities between the two kinds of eigenvalues of a linear transformation, Proc. Nat. Acad. Sci. U. S. **35,** 408–411 (1949).
[9] K. Fan, On a theorem of Weyl concerning eigenvalues of linear transformations I, Proc. Nat. Acad. Sci. U. S. **35,** 652–655 (1949).

WASHINGTON, July 28, 1953.

Journal of Research of the National Bureau of Standards Vol. 52, No. 1, January 1954 Research Paper 2468

Prediction of the Likelihood of Interference at Frequencies of 30 to 42 Megacycles in Alaska

T. N. Gautier, Jr., and C. J. Sargent

The likelihood of interference with very-high-frequency networks in Alaska from stations operating on similar frequencies in other parts of the world, as a function of season, sunspot number, and time of day, is presented. This example serves as a model for similar computations for other communication links. Calculations are based upon regular reflection from the *F*2 layer, and data are supplied for estimating the probability of interference from sporadic-*E* reflections.

1. Introduction

At the request of the Civil Aeronautics Administration a study was made of the likelihood of interference with the operation of a proposed very-high-frequency line-of-sight network in Alaska caused by ionospheric propagation of signals between stations within the network and of signals from distant stations outside the network. The study was made for operating frequencies of 30, 36, and 42 Mc. The likelihood of interference at these frequencies is inferred from the likelihood of occurrence of maximum usable frequencies (MUF) equal to or greater than these frequencies calculated for propagation paths between stations within the network and between distant points and two representative points in the network.

This specific study is an example of a communication problem of general interest, and is presented in full to serve as a guide in solving similar problems.

Nome, Alaska, and Annette Island, Alaska, near the extremes of the network, were chosen as the points within the network for the study of interference from distant stations.

The likelihood of the MUF exceeding 30, 36, and 42 Mc was calculated for three classes of propagation paths: (1) *F*2-layer paths from stations at distances greater than 4,000 km from Nome and Annette Island, respectively. (2) *F*2-layer paths less than 4,000 km in length, including paths between network stations. (3) Sporadic-*E* paths between stations of the network.

2. Basic F2-4000 MUF Prediction Charts

Using standard procedures, *F*2-4000 MUF contour charts similar to those appearing in the CRPL–D series [1] [1] were drawn for latitudes 30° to 70° north in the I-zone, for sunspot numbers 60, 80, 100, 120, and 140, and the months June and December. It was not necessary to prepare charts for sunspot numbers less than 60 for the problem under consideration.

Sunspot numbers referred to are 12-month averages of relative sunspot numbers. The average maximum 12-month average sunspot number for the past 10 cycles is 105, with a standard deviation of 24. The maximum for the present cycle, which occurred in 1947, was 152.

[1] Figures in brackets indicate the literature references at the end of this paper.

3. Interference from Distant Stations

Using the charts referred to in section 2, figures 1 to 34 were prepared. Figures 1 to 16 are for reception at Nome, whereas figures 17 to 34 are for reception at Annette Island.

Curves on these charts show the predicted variation with sunspot number and time of day of the percentage of occurrence of conditions for reception at 30, 36, and 42 Mc by *F*2-layer propagation from transmitting stations located at distances of 4,000 km and over, in selected azimuth ranges measured clockwise from north at the receiving station. The azimuth ranges for paths terminating at Nome are 53° to 117°, 172° to 254°, and 254° to 299°. The azimuth ranges for paths terminating at Annette Island are 67° to 157°, 218° to 277°, and 277° to 322°. The world areas included in these azimuth ranges are shown in figures 35 and 36. Charts for summer and winter conditions are presented. Charts on which the predicted occurrence is less than 10 percent for sunspot number 140 are omitted. Equinox conditions are approximately intermediate between those for summer and winter.

As an example, in figure 1 the chart for Nome, 30 Mc, June, and azimuth range 53° to 117°, conditions for reception of 30 Mc at 0500 GCT on 90 percent of the days of the month on the average should occur for a sunspot number of 135. For sunspot number 70, reception should occur on only 10 percent of the days on the average at 0500 GCT, whereas for sunspot number 120, reception on 10 percent or more of the days should occur between about 1830 and 0730, with about 75-percent occurrence at 0500.

The charts were constructed as follows:

1. The 2,000-km circle around each receiving station shown in figures 35 and 36, and the selected azimuth intervals, were traced on transparent paper.

2. Daily intervals for reception on more than a specified percentage of days were found by placing these sheets on the predicted 4,000-MUF charts, and noting the earliest and latest times at which the appropriate MUF contour intersected the segment of the 2,000-km circle included in the given azimuth range as the transparency was moved horizontally from left to right across the MUF chart.

For reception on 50 percent of the days, the appropriate contour is that for MUF equal to the given frequency. The dispersion of daily values of

the MUF is such that contours for MUF equal to $1/(1+0.15)$ and $1/(1-0.15)$ times the given frequency correspond approximately to 10- and 90-percent reception, respectively, [2, sec. 6.6, i]. Assuming that the distribution of percentage of MUF is Gaussian, contours for MUF equal to $1/(1+0.08)$ and $1/(1-0.08)$ times the given frequency would then correspond to 25- and 75-percent reception, respectively.

3. Contours in figures 1 to 34 were then plotted by interpolation between the end points of the intervals determined in step 2. Figure 17(b) is discussed below.

Although the predictions are based upon an assumed ring of transmitting stations 4,000 km distant from the receiving station extending over the indicated azimuth range, stations at greater distances in the same azimuth range are also included, provided the MUF at the control point nearest the transmitting station is greater than the given frequency. This will be true, usually, for transmitting stations in the land areas included in the azimuth ranges, except those west of the receiving station during the early hours of the predicted daily reception period, and those east of the receiving station during late hours of the predicted daily reception period, at distances well over 4,000 km.

Actually, portions of the 2,000-km circles around the receiving stations lie outside the I-zone. However, errors introduced by using I-zone predictions for these segments are believed to be less than other uncertainties in the predictions. The error in the position of portions of the curves on these charts may be of the order of 10 or 15 sunspot numbers.

It should be emphasized that these charts show the occurrence of conditions for interference from one or more of a number of distant stations operating on the same frequency and distributed over the entire azimuth range. The interference from a single station would be somewhat less than this. For example, the predicted interference at Annette Island from a station in Washington, D. C., operating at 30 Mc in June is shown in figure 17(b). This may be compared with figure 17(a), which shows the predicted interference from stations throughout the azimuth range 67° to 157°.

4. Interference from Stations Within the Network and Other Stations at Distances Less Than 4,000 Km

Figures 37 to 49 show the predicted occurrence of conditions for interference at 30, 36, and 42 Mc, via *F*2-layer reflections from stations at distances less than 4,000 km as a function of distance and time of day for paths centered on 60° N. latitude, the approximate latitude of the middle of the network. Charts are given for June and December and for sunspot numbers from 60 to 120, in steps of 20. They were prepared by using the MUF values at 60° N. on the *F*2–4000 MUF charts and assuming a ratio of 4000 MUF to zero MUF equal to 2.9, and interpolating by means of the nomogram on page 85 of reference [2]. Conditions for equinoctial months are intermediate between those for summer and winter. When the predicted occurrence was less than 10 percent at all times of the day for distances less than 4,000 km, the chart was omitted.

It may be noted that the predicted occurrence for distances less than 2,000 km, the maximum distance within the network, exceeds 10 percent only in winter near sunspot maximum.

Figure 50 shows the percentage of occurrence by seasons of vertical incidence sporadic-*E* reflections (*fEs*) at frequencies above 7 Mc, observed at Anchorage, Alaska, averaged over 4 years, May 1949 through April 1953. Occurrence of conditions for propagation of 30, 35 and 40 Mc, based on the occurrence of *fEs* above 7 Mc may be estimated as follows:

The logarithm of the probability P of occurrence of vertical incidence sporadic-*E* reflections at frequencies higher than f is roughly a linear function of the frequency [3]. Thus

$$\log_{10} P = a + bf,$$

or

$$\log_{10} (P_1/P_2) = b(f_1 - f_2)$$

$$P_1/P_2 = 10^{b(f_1-f_2)} = B^{(f_1-f_2)}.$$

This does not apply if P is close to 1.0.

Analysis of Anchorage *fEs* measurements indicates that the occurrence of *fEs* above 5 Mc is approximately 2½ times that for *fEs* above 7 Mc. From the preceding relationship $B=(0.4)^{\frac{1}{2}}$, so that $P_f = P_7(0.4)^{(f-7)/2}$ and the probabilities of occurrence of vertical incidence *Es* reflections above 6, 8, 9, 10, and 11 Mc are 1.6, 0.6, 0.4, 0.25, and 0.16, respectively, times the probability of occurrence above 7 Mc.

Assuming regular *E*-layer MUF factors, *Es* MUF equal to 30, 35, and 40 Mc, corresponds approximately to *fEs* equal to 6, 7, and 8 Mc, respectively, for a distance of 2,000 km, to *fEs* equal to 7, 8, and 9 Mc, respectively, for a distance of 1,500 km, and to *fEs* equal to 9, 10, and 11 Mc, respectively, for a distance of 1,000 km.

The approximate relative frequencies of occurrence of *Es* MUF greater than 30, 35, and 40 Mc, for distances of 1,000, 1,500, and 2,000 km (i. e., ratios to the occurrence of *fEs* above 7 Mc), based on the above relations, are summarized in table 1.

Referring again to figure 50, Anchorage *fEs* above 7 Mc shows little seasonal variation, which is in accord with observations at other stations in the auroral zone. Little is known about the sunspot-cycle variation.

TABLE 1.

Frequency	Distance		
	1,000 km	1,500 km	2,000 km
Mc			
30	0.4	1.0	1.6
35	.25	0.6	1.0
40	.16	.4	0.6

There is reason to doubt the exact quantitative significance of sporadic-E measurements. They should, therefore, be regarded as indicating only roughly the occurrence of conditions for interference at network stations via sporadic-E reflections.

[1] Basic radio propagation predictions, Ntl. Bur. Standards CRPL–D Series, U. S. Government Printing Office, Washington 25, D. C.

[2] Ionospheric radio propagation, NBS Cir. 462, U. S. Government Printing Office, Washington 25, D. C.

[3] M. Lindeman Phillips, Variations in sporadic-E ionization observed at Washington, D. C., Trans. Am. Geophys. Union, **28** 71 (1947).

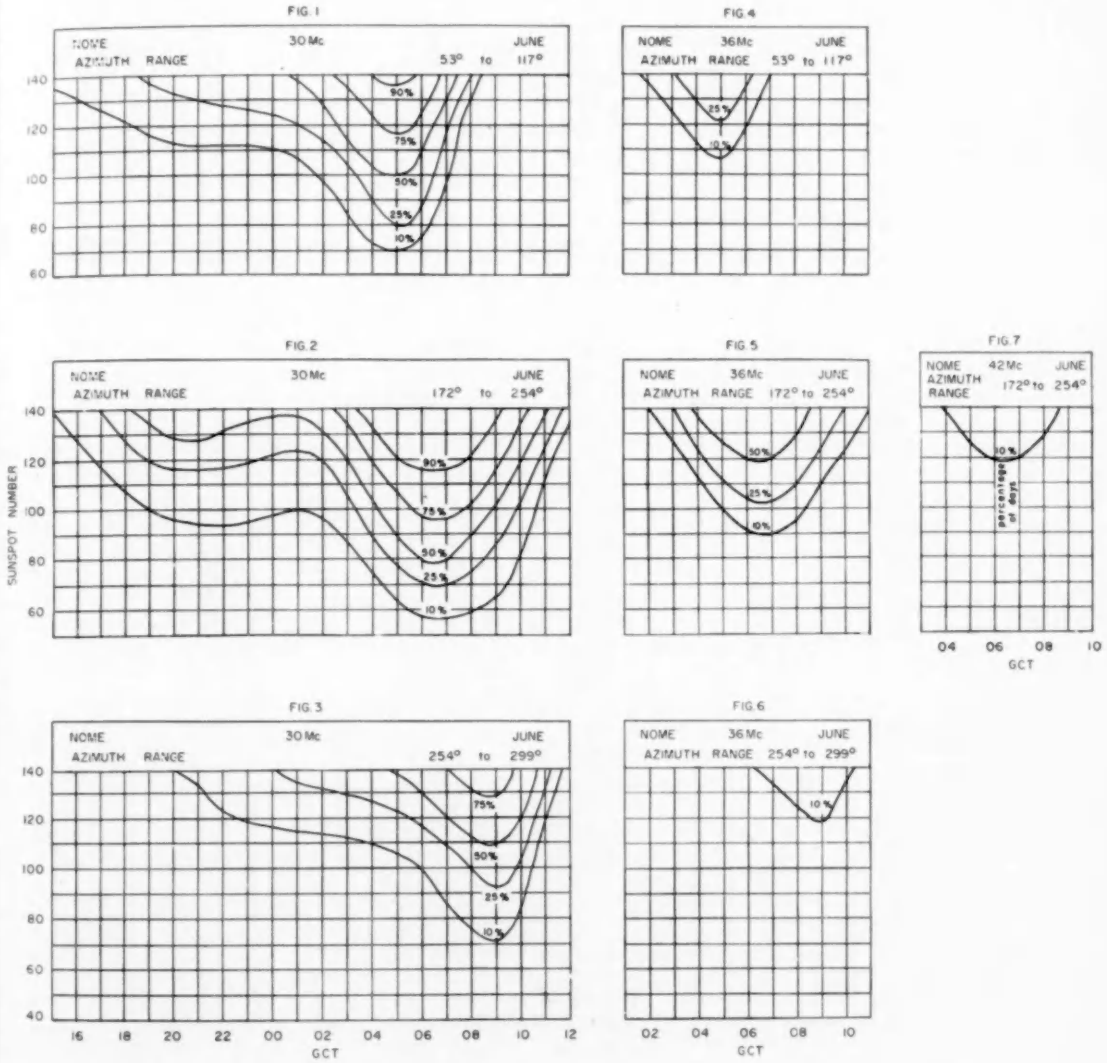

FIGURES 1 to 7. *Predicted occurrence of conditions for reception via F2-layer propagation.*

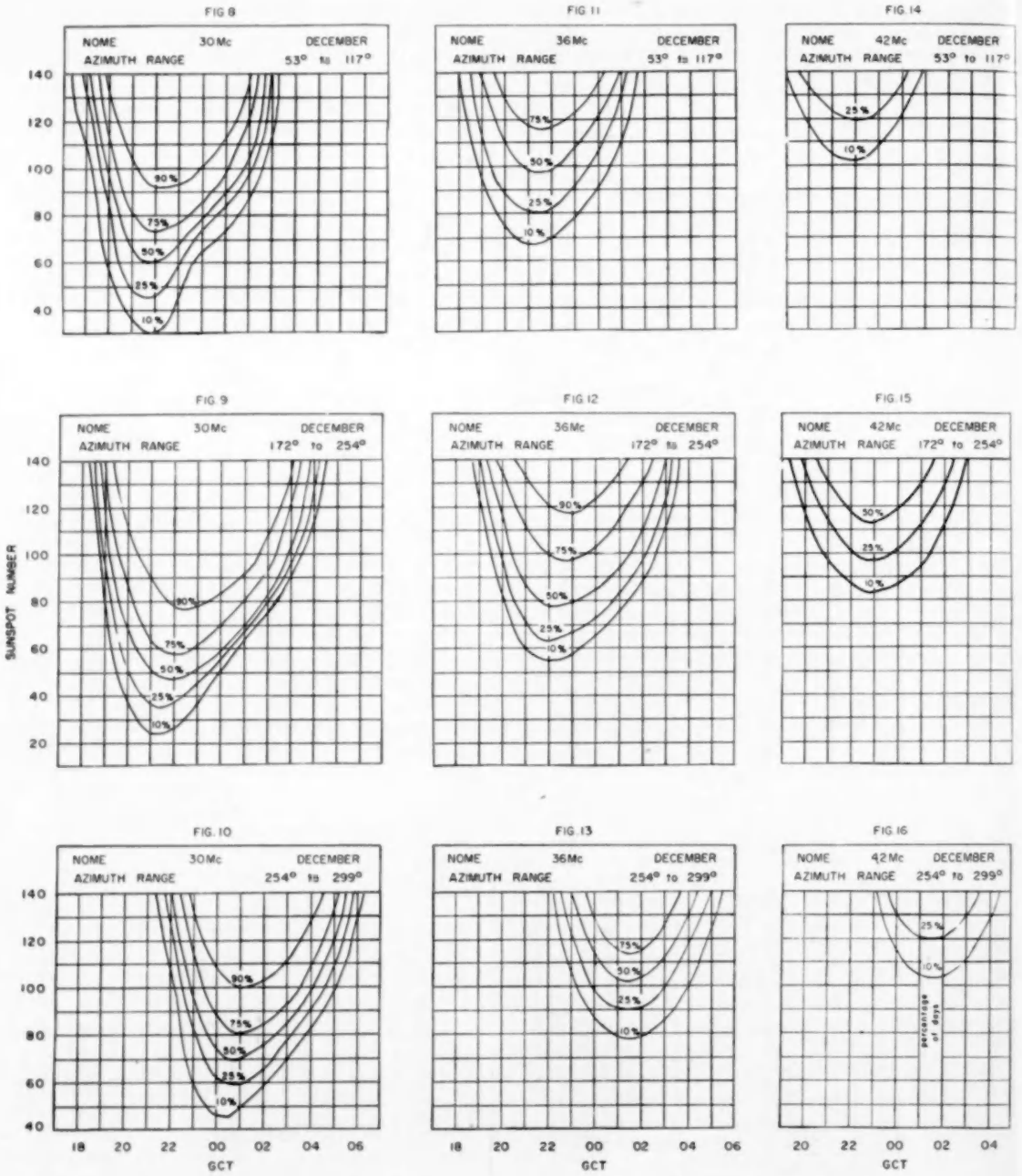

FIGURES 8 to 16. *Predicted occurrence of conditions for reception via F2-layer propagation.*

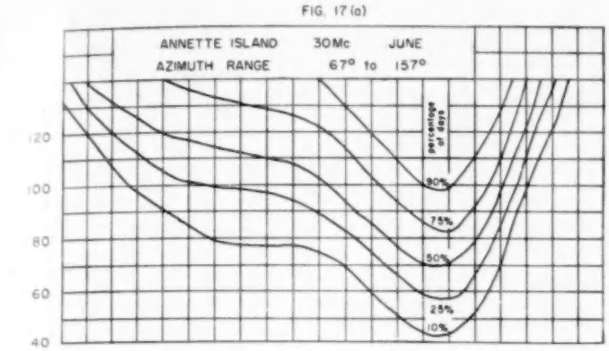

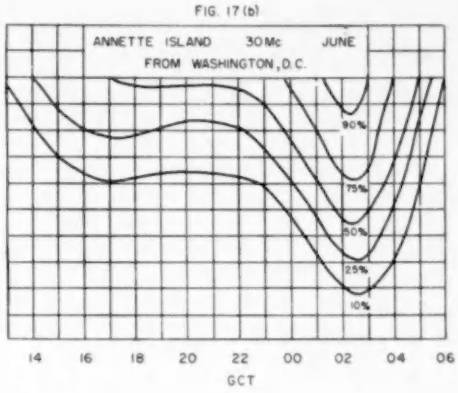

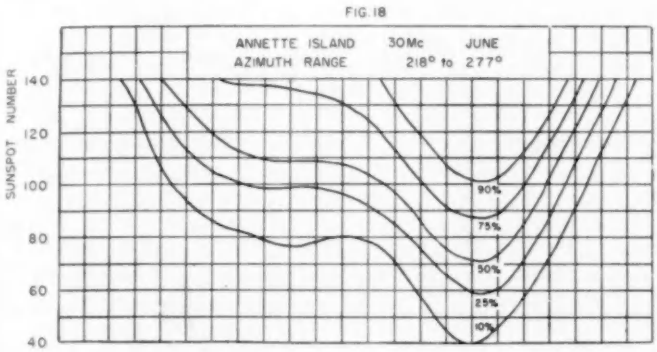

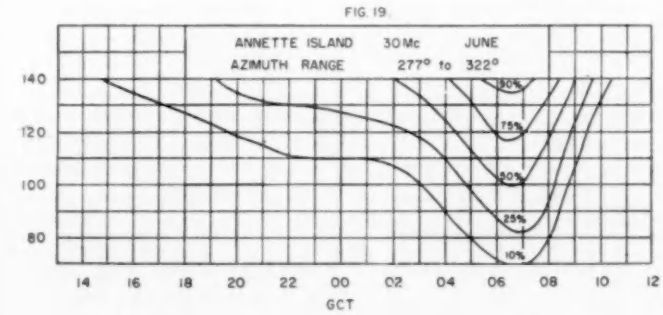

FIGURES 17 to 19. *Predicted occurrence of conditions for reception via F2-layer propagation.*

FIG. 20

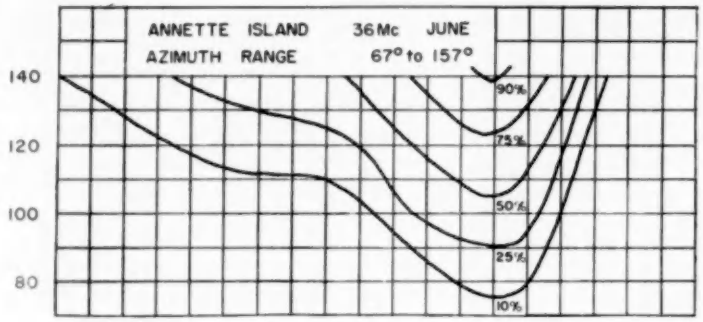

FIG. 23

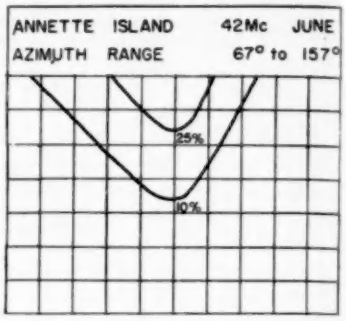

FIG. 21

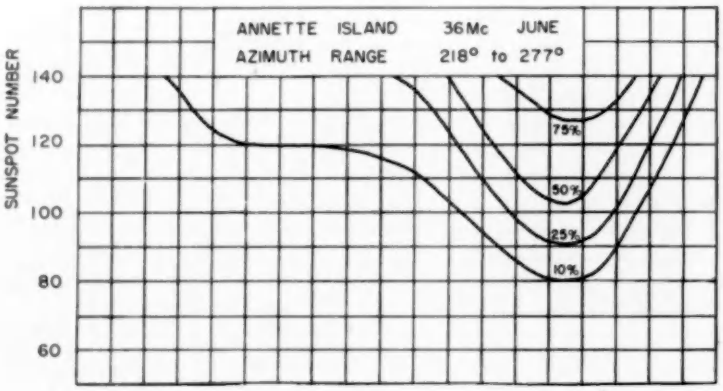

FIG. 24

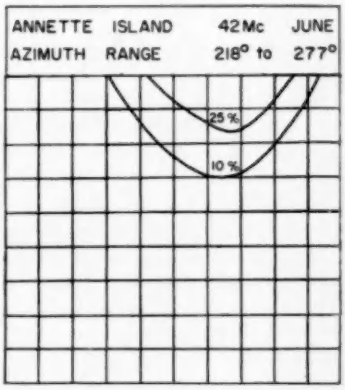

FIG. 22

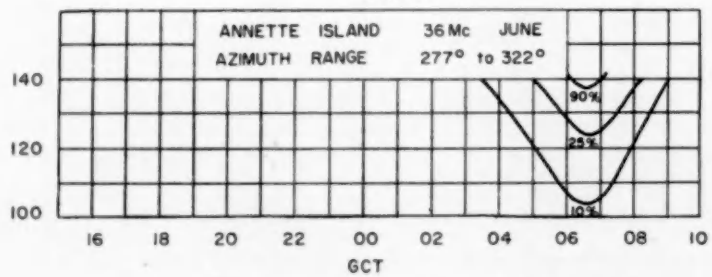

FIG. 25

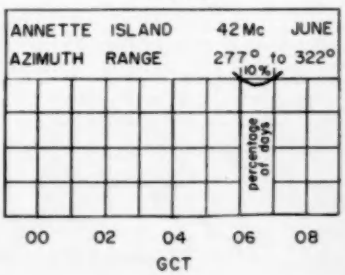

FIGURES 20 to 25. *Predicted occurrence of conditions for reception via F2-layer propagation.*

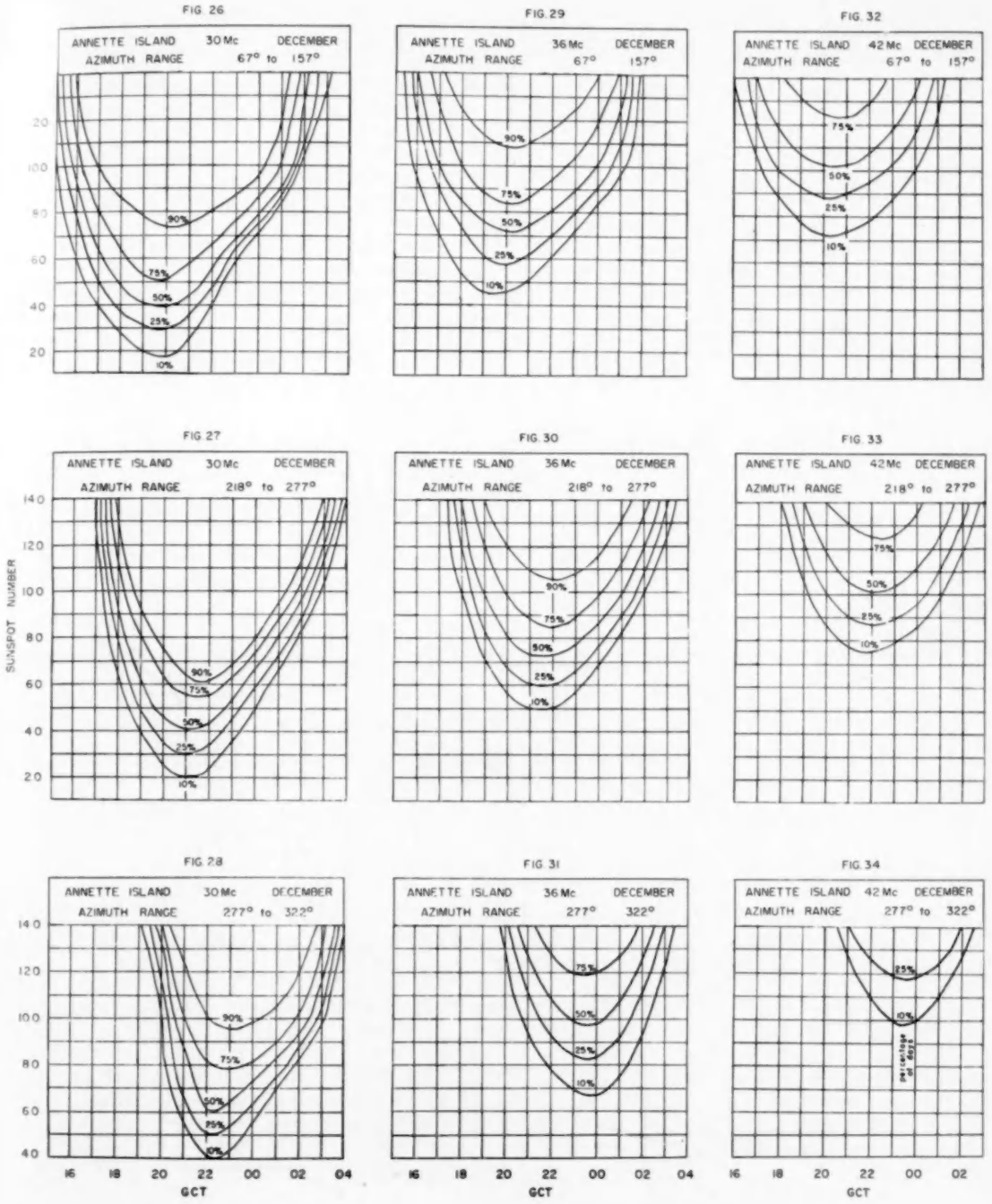

FIGURES 26 to 34. *Predicted occurrence of conditions for reception via F2-layer propagation.*

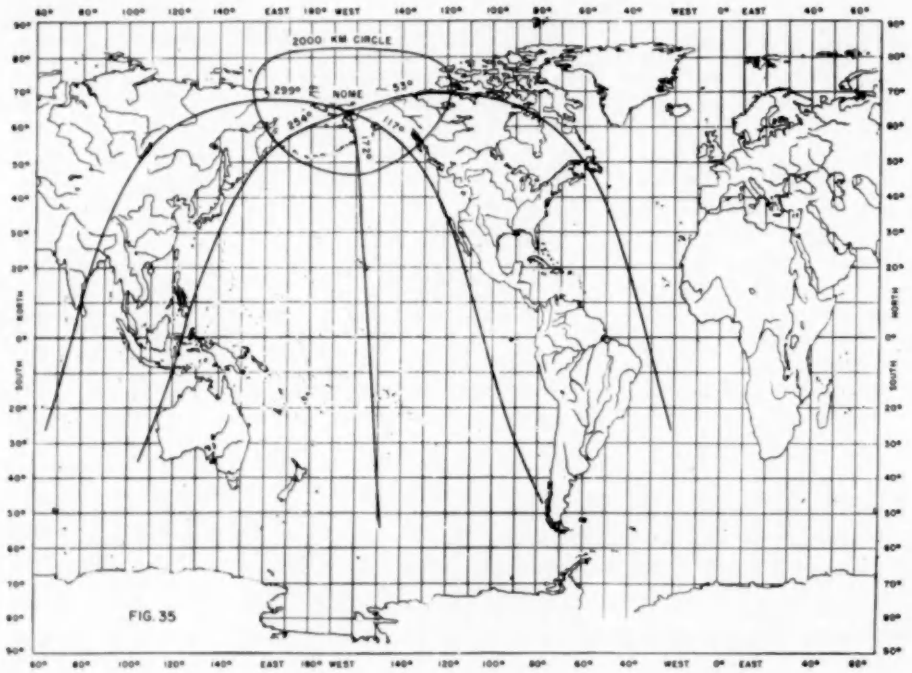

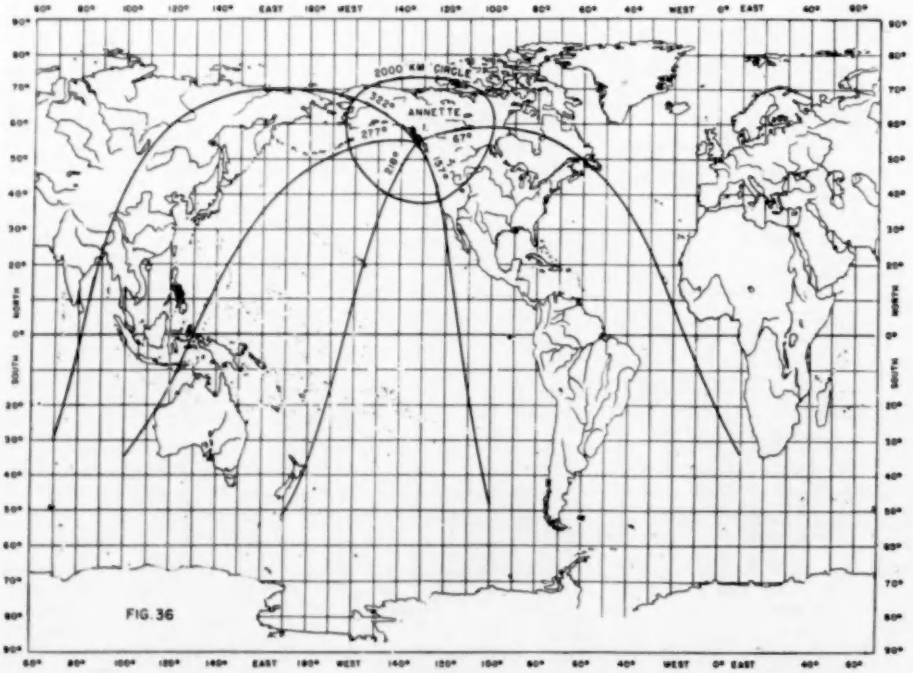

FIGURES 35 and 36. *Maps showing geographical areas included in selected azimuth sectors.*

DISTANCE IN KILOMETERS

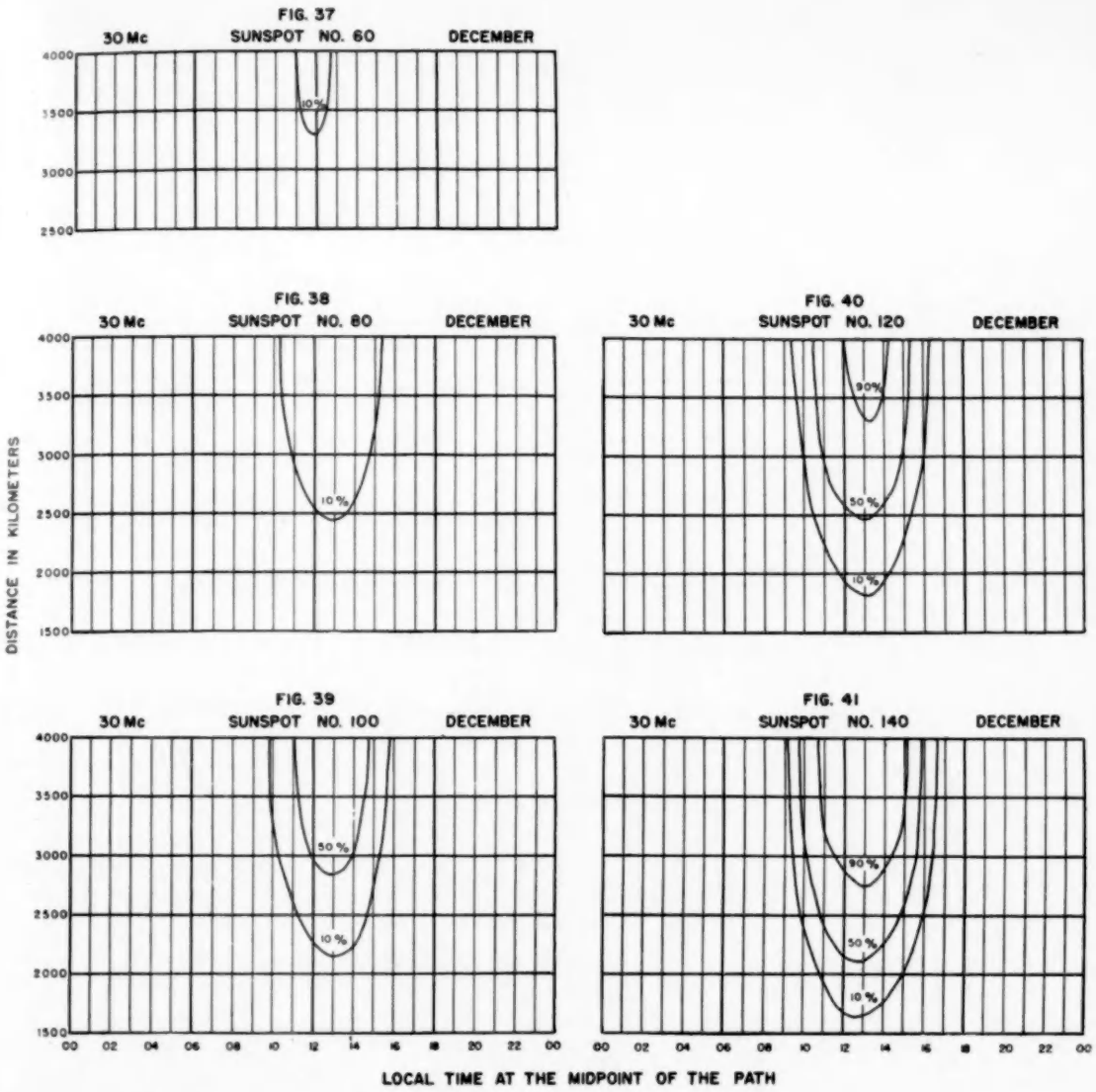

FIGURES 37 to 41. *Predicted skip distance for F2-layer reflection at 60° N. latitude,* I-*zone.*

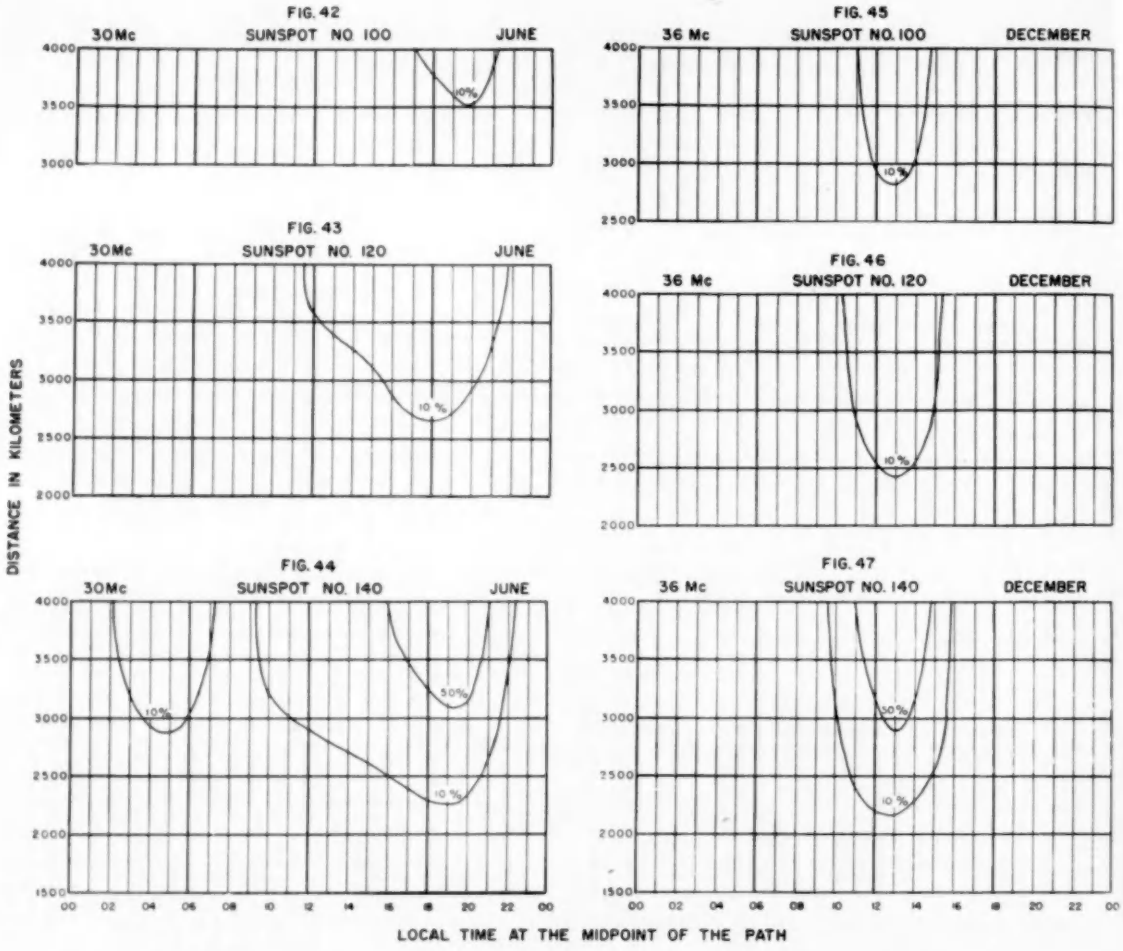

FIGURES 42 to 47. *Predicted skip distance for F2-layer reflection at 60° N. latitude,* I-*zone.*

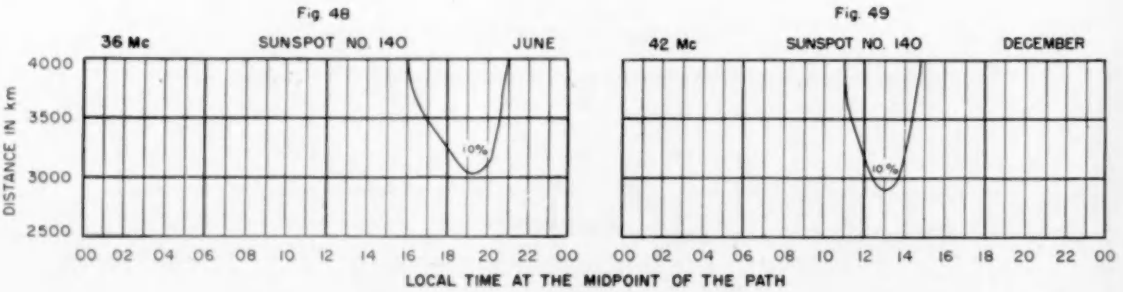

FIGURES 48 and 49. *Predicted skip distance for F2-layer reflection at 60° N. latitude,* I-*zone.*

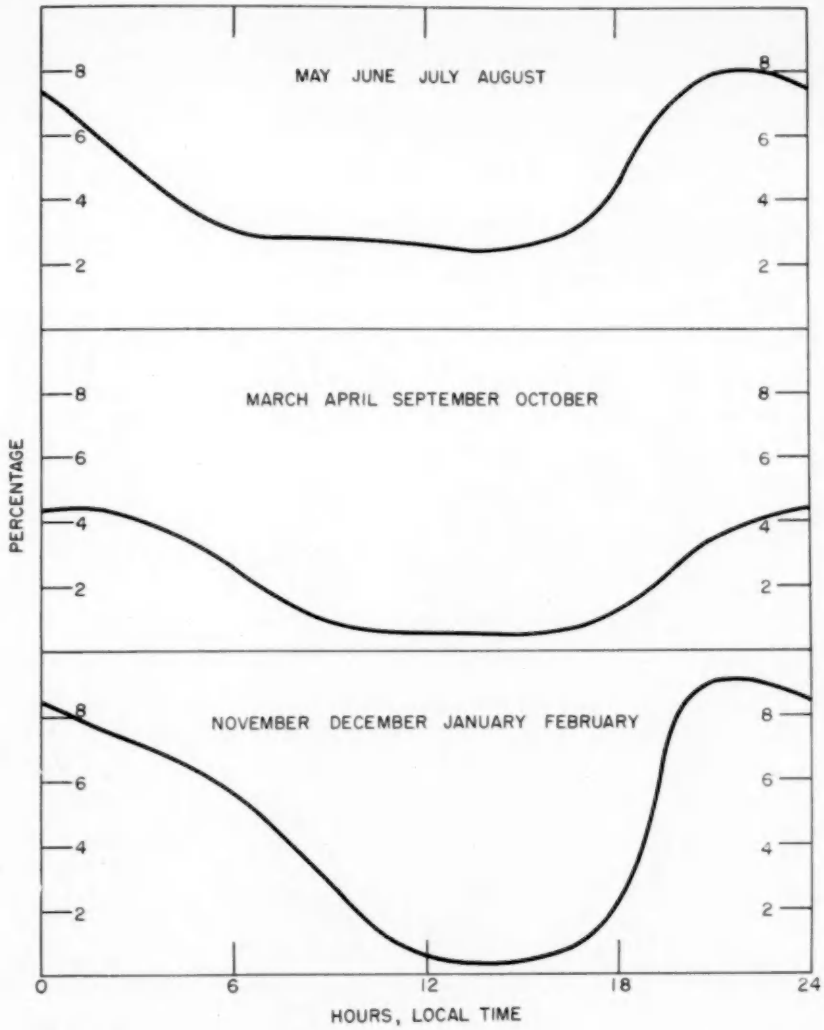

FIGURE 50. *Diurnal variation in percentage of time of occurrence of sporadic E reflections in excess of 7 Mc, Anchorage, Alaska, May 1949–April 1953.*

WASHINGTON, July 1953.

Journal of Research of the National Bureau of Standards Vol. 52, No. 1, January 1954 Research Paper 2469

Tables for Use in the Interpretation of Paramagnetic Behavior Below 1° K; for the Chromic Alums (J=3/2)

Ralph P. Hudson and Charles K. McLane

The method of interpreting susceptibility and entropy data, obtained in adiabatic demagnetization experiments, by means of the theory of Hebb and Purcell in order to derive absolute temperatures is recounted briefly. This forms an introduction to tables that enable one to carry out this procedure for the case of the chromic alums.

The low-temperature behavior of the chromic alums is largely determined by the fact that the fourfold degenerate ground level of the Cr^{+++} ion is split by the crystalline electric field (Stark effect) into two doublets separated by an energy δ. The theory of Hebb and Purcell [1] [1] yields expressions for the susceptibility, χ_0, and the entropy, S, as functions of the absolute temperature, T, and this splitting δ. Thus one may obtain a relation between S and χ_0 for any chosen δ. In practice one usually employs the "magnetic temperature" T^* instead of χ_0, and $T^*=c/\chi_0$, where c is the Curie constant per cubic centimeter.

Now experiment also leads to a χ_0 versus S (or T^* versus S) relation, for S may be calculated quite accurately, simply from the conditions of magnetic field and temperature at the beginning of the isentropic demagnetization process, and χ_0 is measured at the end. One therefore has only to find that value of δ which leads to an S versus T^* curve fitting the experimental points. Then over the range of agreement one may suppose the Hebb and Purcell $\chi_0(T)$ and $S(T)$ formulas to be individually correct, and the former leads at once to the establishment of the absolute temperatures.

Table 1 gives, effectively, corresponding values of T/δ and T^*/δ calculated from the Hebb and Purcell formula [1]: $T^*/\delta=\gamma^{-1}\times T/\delta$, where

$$\gamma=\frac{0.2}{1+e^{-\delta/kT}}\left[\left(3+\frac{4kT}{\delta}\right)+\left(3-\frac{4kT}{\delta}\right)e^{-\delta/kT}\right]. \quad (1)$$

Tables 2 to 5 contain the data necessary for calculating the "experimental entropy," that is, in the magnetic field at the initial temperature, and the field-free entropy as a function of kT/δ.

Considering first the case of the entropy in zero field and at low temperatures, two effects contribute to a reduction in the entropy below the "ideal" value of $R \log_e 4$, namely, the Stark splitting and magnetic interaction. The theory treats these two contributions separately, and they are additive. The "Stark entropy" is calculated from the partition function, $Z_e=2(1+e^{-\delta/kT})$, and is given in table 2. Table 3 lists as a function of x (where $x=kT/\delta$), the quantity $(d/dx)(\Omega/x)$, Ω being as defined in reference [1]. The magnetic entropy, S_m, is then given by

$$S_m/R=(\tau/\delta)^2\frac{d}{dx}\left(\frac{\Omega}{x}\right), \quad (2)$$

where $\tau/k=3c(=0.0211$ deg and 0.0194 deg for the potassium and methylammonium alums, respectively). Hence

$$\log_e 4-S/R=(\log_e 4-S/R)_{\text{Stark}}+S_m/R.$$

TABLE 1. *Corresponding values of kT/δ and $k(T^*-T)/\delta$ calculated from the Hebb and Purcell [1] formula: $T^*/\delta=\gamma^{-1}\times T/\delta$ (see text)*

kT/δ	$\frac{T^*-T}{\delta/k}$	kT/δ	$\frac{T^*-T}{\delta/k}$	kT/δ	$\frac{T^*-T}{\delta/k}$
0.05	0.0281$_3$	1.0	0.0312$_2$	3.0	0.0110$_3$
.10	.0470$_8$	1.1	.0287$_2$	3.2	.0103$_8$
.15	.0584$_2$	1.2	.0265$_9$	3.4	.0097$_4$
.20	.0639$_6$	1.3	.0246$_7$	3.6	.0092$_2$
.25	.0653$_4$	1.4	.0230$_3$	3.8	.0087$_1$
.30	.0643$_1$	1.5	.0215$_9$	4.0	.0083$_1$
.35	.0619$_7$	1.6	.0203$_0$	4.2	.0079$_0$
.40	.0590$_3$	1.7	.0191$_7$	4.4	.0075$_4$
.45	.0558$_8$	1.8	.0181$_4$	4.6	.0072$_2$
.50	.0527$_1$	1.9	.0172$_2$	4.8	.0069$_2$
.55	.0497$_1$	2.0	.0163$_9$	5.0	.0066$_4$
.60	.0469$_3$	2.1	.0156$_3$		
.65	.0443$_2$	2.2	.0149$_6$		
.70	.0419$_2$	2.3	.0143$_1$		
.75	.0397$_5$	2.4	.0137$_3$		
.80	.0377$_8$	2.5	.0131$_8$		
.85	.0359$_1$	2.6	.0127$_0$		
.90	.0342$_3$	2.7	.0122$_7$		
.95	.0326$_8$	2.8	.0118$_6$		
1.00	.0312$_2$	2.9	.0113$_9$		
		3.0	.0110$_3$		

[1] Figures in brackets indicate the literature references at the end of this paper.

TABLE 2. *"Stark entropy", or the reduction in entropy below the value $R \log_e 4$, caused by the effect of the crystal field*

kT/δ	$\log_e 4-S/R$	kT/δ	$\log_e 4-S/R$	kT/δ	$\log_e 4-S/R$
0	0.6931$_3$	1.0	0.1109$_4$	3.0	0.0137$_0$
0.05	.6931$_3$	1.1	.0935$_3$	3.2	.0120$_8$
.10	.6926$_1$	1.2	.0798$_1$	3.4	.0107$_6$
.15	.6834$_0$	1.3	.0688$_3$	3.6	.0095$_5$
.20	.6529$_7$	1.4	.0599$_5$	3.8	.0085$_4$
.25	.6030$_2$	1.5	.0526$_2$	4.0	.0077$_5$
.30	.5432$_8$	1.6	.0465$_4$	4.2	.0070$_4$
.35	.4821$_2$	1.7	.0414$_2$	4.4	.0064$_2$
.40	.4246$_1$	1.8	.0371$_4$	4.6	.0058$_7$
.45	.3729$_8$	1.9	.0334$_2$	4.8	.0054$_0$
.50	.3278$_1$	2.0	.0303$_0$	5.0	.0049$_8$
.55	.2888$_1$	2.1	.0275$_9$		
.60	.2553$_9$	2.2	.0251$_7$		
.65	.2267$_0$	2.3	.0230$_9$		
.70	.2021$_4$	2.4	.0212$_4$		
.75	.1810$_4$	2.5	.0196$_3$		
.80	.1628$_4$	2.6	.0181$_5$		
.85	.1470$_9$	2.7	.0168$_6$		
.90	.1333$_9$	2.8	.0156$_9$		
.95	.1214$_2$	2.9	.0146$_3$		
1.00	.1109$_4$	3.0	.0137$_0$		

282952—54——3

TABLE 3. *Corresponding values of kT/δ and the function $(d/dx)(\Omega/x)$* [1]

The "magnetic entropy", S_m, or the entropy diminution additional to the Stark entropy (table 2), is obtained from the relation $S_m/R=(\tau/\delta)^2(d/dx)(\Omega/x)$, (see text).

kT/δ	$\frac{d}{dx}\left(\frac{\Omega}{x}\right)$	kT/δ	$\frac{d}{dx}\left(\frac{\Omega}{x}\right)$	kT/δ	$\frac{d}{dx}\left(\frac{\Omega}{x}\right)$
0	.....	1.0	0.7706$_8$	3.0	0.1228$_3$
0.05	.....	1.1	.6795$_1$	3.2	.1090$_2$
.10	7.1616$_7$	1.2	.6005$_8$	3.4	.0971$_3$
.15	2.9618$_7$	1.3	.5327$_1$	3.6	.0871$_9$
.20	1.4571$_8$	1.4	.4745$_1$	3.8	.0785$_2$
.25	0.9478$_8$	1.5	.4245$_9$	4.0	.0711$_4$
.30	.8777$_7$	1.6	.3817$_0$	4.2	.0647$_4$
.35	.9611$_8$	1.7	.3444$_3$	4.4	.0591$_7$
.40	1.0705$_6$	1.8	.3122$_3$	4.6	.0542$_9$
.45	1.1518$_7$	1.9	.2841$_1$	4.8	.0498$_8$
.50	1.1940$_8$	2.0	.2595$_9$	5.0	.0461$_4$
.55	1.2007$_8$	2.1	.2378$_8$		
.60	1.1820$_8$	2.2	.2187$_4$		
.65	1.1451$_3$	2.3	.2017$_3$		
.70	1.0967$_6$	2.4	.1866$_7$		
.75	1.0425$_8$	2.5	.1731$_3$		
.80	0.9857$_3$	2.6	.1610$_6$		
.85	.9292$_0$	2.7	.1503$_8$		
.90	.8738$_9$	2.8	.1402$_2$		
.95	.8208$_8$	2.9	.1313$_6$		
1.00	.7706$_8$	3.0	.1228$_3$		

Table 4 lists values of the entropy, for corresponding values of H/T, calculated by means of the "Brillouin formula." For the case $J=3/2$, one has

$$(S/R)_B=a\coth a-4a\coth 4a+\log_e\sinh 4a-\log_e\sinh a, \quad (3)$$

where $a=\mu H/kT$; μ is the Bohr magneton, 9.271×10^{-21} emu, and k is the Boltzmann constant, 1.3805×10^{-16} erg deg^{-1}.

In order to derive an accurate value of δ, however, one must take cognizance of the fact that the Brillouin entropy (table 4) is only appropriate to the ideal case of a fourfold degenerate ground level. The effect of the crystalline electric field is to modify the pattern of the level splitting in a magnetic field, and for small fields the correction, $\Delta S/R$, to be applied to the entropy reduction, $\log_e 4-S_B/R$, is relatively large.

An entropy formula has been derived [3] that takes this effect into account, but it is more unwieldy than the Brillouin formula (a straightforward function of H/T) as it is a function of H, T, and δ. For the chromic alums the value of δ/k is always close to 0.25 deg, and starting temperatures (that is, bath temperatures) will, in general, be of the order of 1.1° to 1.2° K. Because $\Delta S/R \ll S_B/R$, the Brillouin and exact entropy curves run very close together, and the following approximate method of calculating a new $\Delta S/R$ under slightly changed conditions of δ and/or T (say δ_1, T_1), given a table of exact values for conditions δ_0, T_0, is found to be very useful.

Let $\Delta=\delta/2$, $\alpha=\Delta/T$, and $\beta=\mu H/\Delta$. One may then take the expressions for both the Brillouin entropy and the exact entropy and obtain their derivatives with respect to α. Denoting derivatives by a primed symbol, we then have

$$(S_B/R)_\alpha \approx (S_B/R)_{\alpha_0}+(S'_B/R)_{\alpha_0}\times(\alpha-\alpha_0), \quad \text{(Brillouin)} \quad (4)$$

and

$$(S/R)_\alpha \approx (S/R)_{\alpha_0}+(S'/R)_{\alpha_0}\times(\alpha-\alpha_0). \quad \text{(exact)} \quad (5)$$

Subtracting (5) from (4)—for a positive quantity—we find

$$(\Delta S/R)_\alpha=(\Delta S/R)_{\alpha_0}+(\Delta S'/R)_{\alpha_0}\times(\alpha-\alpha_0) \quad (6)$$

to a satisfactory degree of accuracy. It must be emphasized that eq (4) and (5) are only approximate. Higher derivatives have been neglected, but these effectively disappear in the subtraction, which leads to eq (6).

In table 5 the entropy values have been calculated for various values of H, and with $\delta/k=0.27$ deg,

TABLE 4. *Entropy as a function of $a(=\mu H/kT)$ calculated from the "Brillouin formula": $S/R=a\coth a-4a\coth 4a+\log_e\sinh 4a-\log_e\sinh a$*

Tables for $J=1/2$, 3/2, 5/2, 7/2 can be found in an article by Hull and Hull [2]; the greater part of table 1 has been taken from this source.

a	S/R	$\log_e 4-S/R$	a	S/R	$\log_e 4-S/R$	a	S/R	$\log_e 4-S/R$
0	1.38629	0	0.40	1.07179	0.3145	1.50	0.20817	1.1781
0.01	1.38604	0.0003	.45	1.00961	.3767	1.55	.19228	1.1940
.02	1.38530	.0010	.50	0.94754	.4387	1.60	.17756	1.2087
.03	1.38405	.0022	.55	.88658	.4997	1.65	.16393	1.2224
.04	1.38231	.0040	.60	.82750	.5588	1.70	.15131	1.2350
.05	1.38007	.0062	.65	.77083	.6155	1.75	.13963	1.2467
.06	1.37735	.0089	.70	.71690	.6694	1.80	.12882	1.2575
.07	1.37415	.0121	.75	.66591	.7204	1.85	.11882	1.2675
.08	1.37047	.0158	.80	.61796	.7683	1.90	.10957	1.2767
.09	1.36632	.0200	.85	.57303	.8133	1.95	.10102	1.2853
.10	1.36171	.0246	.90	.53102	.8553	2.00	.09311	1.2932
.12	1.35115	.0351	.95	.49185	.8944	2.1	.07904	1.3072
.14	1.33887	.0474	1.00	.45543	.9309	2.2	.06705	1.3192
.16	1.32496	.0613	1.05	.42156	.9647	2.3	.05681	1.3295
.18	1.30952	.0768	1.10	.39011	.9962	2.4	.04809	1.3382
.20	1.29266	.0936	1.15	.36091	1.0254	2.5	.04068	1.3456
.22	1.27449	.1118	1.20	.33382	1.0525	2.6	.03438	1.3519
.24	1.25514	.1311	1.25	.30871	1.0776	2.7	.02903	1.3573
.26	1.23471	.1516	1.30	.28543	1.1009	2.8	.02449	1.3618
.28	1.21334	.1730	1.35	.26386	1.1224	2.9	.02064	1.3656
.30	1.19115	.1951	1.40	.24386	1.1424	3.0	.01739	1.3689
.32	1.16824	.2181	1.45	.22534	1.1609			
.34	1.14475	.2415	1.50	.20817	1.1781			
.36	1.12077	.2655						
.38	1.09642	.2899						
.40	1.07179	.3145						

$T=1.1°$ K (the Brillouin entropy itself is, of course, independent of δ, but the values of H are listed in terms of $\mu H/\Delta$, which appears in the analytical expressions for the exact entropy). We thus have $\Delta=0.135$ and $\alpha_0=0.1227273$. The derivatives are given in columns 3 and 5.

Now, in any experiment, T is determined by experimental conditions, and δ is usually known fairly accurately. (It is not illogical to derive an accurate value of δ from entropy data, the calculation of which involves δ; it is essentially the method of successive approximation.) These together fix the value of α, and a tabulation of $\Delta S/R$ is readily obtained by making use of table 5 and eq (6).

One then plots a curve of $\Delta S/R$ versus $(S_B/R)_\alpha$ (using eq (4)) to obtain the correction curve appropriate to one's own experimental conditions. For any one demagnetization, S_B/R is readily obtained from the H/T value and table 1, and $\Delta S/R$ is read off from the correction curve.

TABLE 5. *Brillouin entropy, entropy correction, and first derivatives with respect to* $\alpha(=\Delta/T)$ *for the "standard value"* α_0 *of* 0.1227273 $(=0.135/1.1)$, *for varying values of* $\beta(=\mu H/\Delta)$. $\Delta=\delta/2$ (*see text*)

$\beta=\mu H/\Delta$	$(S_B/R)_{\alpha_0}$	$-(S'_B/R)_{\alpha_0}$	$(\Delta S/R)_{\alpha_0}$	$(\Delta S'/R)_{\alpha_0}$
0	1.38629	0	0.00747	0.1209
0.4	1.38029	0.097397	.00744	.1197
.8	1.36259	.380323	.00734	.1162
1.2	1.33400	.821912	.00716	.1110
1.9	1.26186	1.856246	.00674	.0983
2.8	1.14042	3.337499	.00605	.0790
3.7	1.00451	4.610410	.00529	.0600
4.6	0.86918	5.478282	.00451	.0435
6.0	.67952	6.036330	.00350	.0238
7.5	.51466	5.909656	.00260	.0097
9.0	.38737	5.417034	.00191	.0010
10.5	.29057	4.787534	.00137	−.0038
12.0	.21734	4.128350	.00093	−.0022

To illustrate the efficiency of the method, table 6 lists values of $\Delta S/R$ calculated rigorously and by the above approximation for the case $\alpha=0.113043$ ($\delta=0.26$ deg, $T=1.15°$ K) and for the case $\alpha=0.133333$ ($\delta=0.28$ deg, $T=1.05°$ K). Inasmuch as one is only interested in an accuracy to the fourth decimal place, or two significant figures, it may be seen that the method is very useful.

TABLE 6. *Comparison of entropy-correction values calculated exactly and by the approximate method for the cases (a)* $\alpha=0.113043$ $(\delta/k=0.26$ *deg,* $T=1.15°K)$, *and (b)* $\alpha=0.133333$ $(\delta/k=0.28$ *deg,* $T=1.05°K)$

$\beta=\mu H/\Delta$	$\alpha=0.133333$		$\alpha=0.113043$	
	$\Delta S/R$ (exact)	$\Delta S/R$ (approx.)	$\Delta S/R$ (exact)	$\Delta S/R$ (approx.)
0	0.0088_1	0.0087_6	0.0063_5	0.0063_0
3.7	$.0059_9$	$.0059_2$	$.0047_0$	$.0047_9$
10.5	$.0013_2$	$.0013_3$	$.0013_9$	$.0014_1$

[1] M. H. Hebb and E. M. Purcell, J. Chem. Phys. **5**, 338 (1937).
[2] J. R. Hull and R. A. Hull, J. Chem. Phys. **9**, 465 (1941).
[3] R. P. Hudson, Phys. Rev. **88**, 570 (1952).

WASHINGTON, September 17, 1953.

Journal of Research of the National Bureau of Standards Vol. 52, No. 1, January 1954 Research Paper 2470

Phase Equilibrium Relations in the Systems Lime-Titania and Zirconia-Titania

L. W. Coughanour, R. S. Roth, and V. A. DeProsse

The systems CaO-TiO_2 and ZrO_2-TiO_2 were studied by means of solid-state reactions and by the observation of fusion characteristics. The existence of two binary compounds in the CaO-TiO_2 system was confirmed. One compound was found to exist in the ZrO_2-TiO_2 system. This compound, ZrO_2-TiO_2, has been found to have orthorhombic symmetry with the following parameters at room temperature: $a=4.806$ A, $b=5.032$ A, $c=5.447$ A. Solid-solution development was observed in the ZrO_2-TiO_2 system, but not in the CaO-TiO_2 system. From the data obtained, an equilibrium diagram is suggested for each system.

I. Introduction

A study of phase relationships in the systems CaO-TiO_2 and ZrO_2-TiO_2 has been conducted as a part of a program of fundamental studies of ceramic dielectrics.[1] Both of these systems have been investigated by previous workers. The results of these investigations were rather divergent, however, so it was considered essential that the systems be reinvestigated.

The number of compounds proposed for the CaO-TiO_2 system has varied from one [1][2] to three [2]. Some previous studies of the ZrO_2-TiO_2 system [3, 4] have indicated the absence of any compounds in the system and the presence of partial solid solutions. The possibility of the stabilization of the tetragonal form of ZrO_2 by TiO_2 has also been suggested [5]. Brown and Duwez [6] from X-ray and thermal-expansion measurements proposed a phase diagram indicating the compound ZrO_2-TiO_2. Their diagram, although not supported by fusion-point data, is similar to the one determined in the present investigation.

The determination of the melting points of the compounds, and of the solidus and liquidus temperatures at various points across the two systems, have supplied data from which a revised equilibrium diagram has been constructed for the systems CaO-TiO_2 and ZrO_2-TiO_2.

2. Sample Preparation and Test Methods

The following materials were used as the source of components in the samples for this study: CaO—Eimer Amend Co. reagent-grade calcium carbonate of 99.5-percent purity; ZrO_2—dense ZrO_2 of nominal 99-percent purity, obtained from the Titanium Alloy Manufacturing Co.; TiO_2—highly purified titania of purity over 99.9-percent, obtained from the Titanium Division of the National Lead Co.

Calculations of weight composition were made to ± 0.01 percent, no correction being made for the percentage purity of the raw materials.

The components, in sufficient quantities to give a 10-g sample, were weighed to the nearest milligram. They were then mixed with a binder of either a 5-percent soluble-starch solution or a saturated solution of paraffin in carbon tetrachloride, and 1-in.-diam disks were formed at a pressure of 5,000 lb/in.^{2}. The pressed samples were fired for 4 hr at 1,200° C on platinum foil in an air atmosphere, using an electrically heated furnace wound with 80 Pt–20 Rh wire. The disks were cooled and then ground, repressed, and refired for 4 hr at 1,350° C, again under oxidizing conditions. X-ray examination of the samples showed, after these two heat treatments, that the solid-phase reactions were essentially complete with the exception of the formation of $3CaO{\cdot}2TiO_2$. The composition representing this compound was a mixture of CaO and CaO-TiO_2 after these two calcinations. However, upon heating to 1,560° C, or higher, the reaction to form the compound $3CaO{\cdot}2TiO_2$ took place quite readily.

Following this preliminary heat treatment the disks were ground, remixed with starch-solution binder, and disks about ¼ in. high were formed at 15,000 lb/in.^{2} in a ½-in.-diam mold. From these disks, the specimens for solidus and liquidus determinations were ground in the form of small four-sided pyramids, grooved on each side [7]. The tests were conducted in a thoria resistor-type furnace [8, 9]. The specimens were placed in the furnace on a disk of a platinum-rhodium alloy for temperatures below 1,900° C. For temperatures higher than this value, the samples were placed on an iridium disk. The metal disk was on a support of ThO_2. The heating rate during the tests was about 4 deg C/min until the solidus temperature was approached, when it was reduced to about 2 deg C/min, or less. There was an oxidizing atmosphere in the furnace at all times. The temperature and fusion characteristics of the specimens were observed with an optical pyrometer calibrated at the National Bureau of Standards. In the determination of the solidus and liquidus temperatures, the first sign of liquid formation, rounding of the corners of the test pyramid, was recorded as the solidus temperature. The

[1] This study was sponsored by the Office of Ordnance Research, Department of the Army.

[2] Figures in brackets indicate literature references at the end of this paper.

temperature of complete melting, as arrived at by observations through the optical pyrometer and by visual inspection of the cooled specimen, was recorded as the liquidus temperature. In all cases, several tests had to be made to determine these two values.

The determination of such temperatures is subject to a number of sources or error. Among these are the slight deviations from blackbody conditions, the introduction of small quantities of impurities into the specimens in the forming and grinding operations, the possibility of reduction of TiO_2 at high temperatures, and the inherent difficulty in the visual determination of the solidus and liquidus temperatures. In the present study, care was taken to keep each of these possible errors to a minimum. It is believed that the temperatures as recorded are accurate to $\pm 10°$ C.

After the fused specimens had cooled, they were analyzed either petrographically or by means of X-ray powder patterns, using a high-angle recording spectrometer, and Cu Kα radiation. All X-ray data are reported as observed, uncorrected for temperature or adsorption characteristics. Similar analyses were performed on specimens that had been quenched from temperatures up to 1,600° C.

3. The CaO-TiO_2 System

A considerable amount of work has been done on this system by previous investigators. The results, however, have been in rather serious disagreement, and the present study was undertaken to determine the correct equilibrium relations.

Tanaka [1] decided that there is only one compound, CaO-TiO_2, in the system and that CaO forms solid solutions with this compound. Hedvall and Anderson [10], by means of X-ray studies of samples fired to a maximum temperature of 1,135° C, also concluded that CaO-TiO_2 is the only compound in the system. H. von Wartenberg, et al. [2] published a liquidus curve for the system which indicated the existence of three congruently melting compounds, $3CaO$-TiO_2, $2CaO$-TiO_2, and CaO-TiO_2. Several other investigators [11–15] have indicated that the compounds existing in the system are $3CaO$-$2TiO_2$ and CaO-TiO_2. De Vries, et al. [15] proposed a diagram similar to the one here determined.

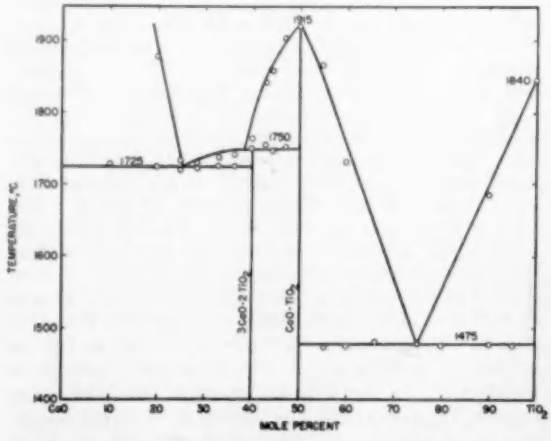

FIGURE 1. *Suggested equilibrium diagram for the system* CaO-TiO_2.

The equilibrium diagram resulting from the present study is shown in figure 1. The fusion-behavior data from which the diagram is constructed are given in table 1. It is seen that there are two compounds in the system. These are CaO-TiO_2 (perovskite), which melts congruently at about 1,915° C, and $3CaO$-$2TiO_2$, which melts incongruently at about 1,750° C. It should be noted that the compound $3CaO$-$2TiO_2$ does not form readily at temperatures below 1,500° C. This may explain why it was not noted by some other investigators. The X-ray powder diffraction pattern for the compound $3CaO$-$2TiO_2$ is given in table 2, but attempts to index this pattern have not, as yet, been successful.

The absence of solid solutions in the diagram should be noted. There is considerable overlapping of some peaks in the diffraction patterns of the compounds CaO-TiO_2 and $3CaO$-$2TiO_2$. This fact makes it rather difficult to unambiguously establish solid-solution relationships by X-ray methods. This difficulty is not present in the petrographic method of analysis, however, as their optical properties differ rather widely. Perovskite has very low birefringence and an index of refraction of about 2.38. The optical properties of the compound $3CaO$-$2TiO_2$ may be tabulated as follows: Optical

TABLE 1. *Fusion characteristics of compositions in the* CaO-TiO_2 *system*

Composition				Results of heating		Results of petrographic or X-ray examination (specimens examined were not quenched and the phases observed may not be those in equilibrium at the liquidus)
Mole		Weight		Solidus	Liquidus	
CaO	TiO_2	CaO	TiO_2			
%	%	%	%	°C	°C	
4.76	95.24	3.39	96.61	1,470	-------	CaO-TiO_2+TiO_2.
10.00	90.00	7.23	92.77	1,470	1,680	Do.
20.00	80.00	14.93	85.07	1,470	-------	Do.
25.00	75.00	18.96	81.04	1,475	-------	Do.
33.33	66.67	25.98	74.02	1,475	-------	Do.
40.00	60.00	31.88	68.12	1,470	1,730	Do.
44.44	55.56	35.96	64.04	1,470	1,850	Do.
50.00	50.00	41.24	58.76	1,915	1,915	CaO-TiO_2.
53.00	47.00	44.18	55.82	1,750	>1,900	CaO-TiO_2+ $3CaO$-$2TiO_2$.
55.56	44.44	46.73	53.27	1,745	1,855	Do.
57.00	43.00	48.20	51.80	1,755	1,840	Do.
60.00	40.00	51.28	48.72	1,755	1,765	$3CaO$-$2TiO_2$.
63.64	36.36	55.12	44.88	1,725	1,740	$3CaO$-$2TiO_2$+CaO.
66.67	33.33	58.39	41.61	1,725	1,735	Do.
71.43	28.57	63.70	36.30	1,720	1,725	Do.
75.00	25.00	67.81	32.19	1,720	1,729	Do.
80.00	20.00	73.73	26.27	1,725	1,870	Do.
90.00	10.00	86.33	13.67	1,725	-------	Do.

character—biaxial (−), $2V \cong 80°$; approximate indices of refraction—$\alpha=2.16$, $\beta=2.20$, $\gamma=2.22$. These values are in good agreement with those in the partial list of optical properties given by Fisk [14].

TABLE 2. *X-ray powder diffraction pattern for the compound* $3CaO \cdot 2TiO_2$

2θ	d	R. I.[a]	2θ	d	R. I.[a]
6.53	13.5	1.4	77.41	1.23	0.8
9.08	9.7	29	77.93	1.22	1.5
13.04	6.8	0.3	78.37	1.22	2.3
18.19	4.9	53	78.78	1.21	1.4
19.63	4.5	2.0	79.00	1.21	0.6
23.63	3.76	1.2	83.72	1.154	.5
26.98	3.30	0.5	85.97	1.129	.8
32.74	2.73	23	86.21	1.127	1.4
32.82	2.73	12	86.57	1.123	0.3
33.05	2.71	10	87.64	1.112	.6
34.36	2.61	0.6	88.94	1.099	.6
36.22	2.48	1.1	90.41	1.085	.2
36.82	2.44	0.8	94.40	1.049	.3
37.08	2.42	.6	96.07	1.036	1.4
37.37	2.40	.5	96.90	1.029	0.9
37.96	2.37	.5	97.34	1.026	.9
38.32	2.35	.3	97.42	1.025	.6
39.61	2.27	.5	101.92	0.9917	1.5
39.95	2.25	1.7	104.32	.9753	10.9
40.03	2.25	1.2	104.86	.9718	0.6
42.58	2.12	0.3	107.09	.9576	.3
43.44	2.08	3.5	107.75	.9536	.5
43.93	2.06	0.5	108.77	.9475	.3
45.03	2.01	.6	113.66	.9202	.8
46.52	1.95	100	114.14	.9177	1.1
47.41	1.92	4.2	114.75	.9145	1.1
48.18	1.89	2.2	115.24	.9121	1.2
50.32	1.81	0.6	115.40	.9112	0.8
51.17	1.78	.9	116.98	.9035	.9
52.67	1.74	.5	117.21	.9021	1.7
53.61	1.71	.5	120.60	.8867	6
55.36	1.66	.6	122.02	.8806	1.2
56.56	1.63	6	124.80	.8692	0.6
58.23	1.58	6	127.23	.8598	.8
58.80	1.57	4.2	128.17	.8564	1.1
63.69	1.46	0.6	128.86	.8539	0.6
64.82	1.44	1.4	132.14	.8427	.8
67.12	1.39	5	138.84	.8228	1.4
68.61	1.37	2.2	139.45	.8211	0.8
69.24	1.36	1.1	140.00	.8197	.6
69.35	1.35	1.5	141.02	.8171	.6
69.91	1.34	0.8	142.79	.8127	3.4
74.23	1.28	.8	146.38	.8046	0.8
76.85	1.24	.8	148.58	.8001	2.2

[a] R. I. is the intensity of diffraction peaks relative to the strongest peak.

4. The ZrO_2-TiO_2 System

A liquidus curve for this system was published by von Wartenberg and Gurr [16]. They showed a eutectic point at about 80 mole percent TiO_2 and 1,760° C. This is in exact agreement with the eutectic determined in the present work. Büssem, Schusterius, and Ungewiss [3] in an X-ray study of the system noted solid-solution development but no compound formation. Sowman and Andrews [4] published a phase diagram for the system Zro_2-TiO_2. Their diagram was one of partial solid solution with no compounds present. They located the eutectic at 45 to 50 weight percent TiO_2 and 1,600° C. This diagram is not in agreement with the one determined in the present work. Later work by Sowman [5] on the ZrO_2-TiO_2 system indicated to him that the 1:1 composition, after heat treatment, consists of either a distorted form of tetragonal ZrO_2 or a new compound. Recently, Brown and Duwez [6] proposed a diagram indicating the existence of the compound ZrO_2-TiO_2. Their diagram is quite similar to the one determined at the Bureau.

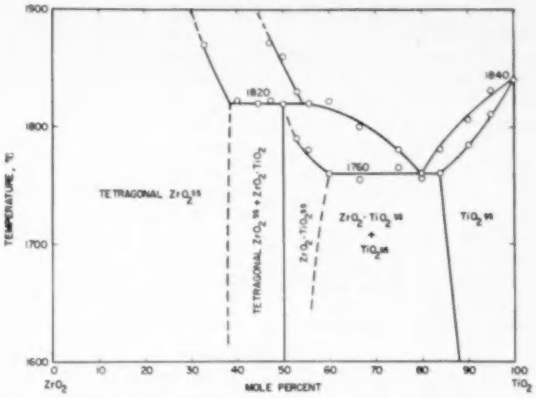

FIGURE 2. *Suggested equilibrium diagram for the system* ZrO_2-TiO_2.

The equilibrium diagram for the ZrO_2-TiO_2 system, as determined in the present study, is shown in figure 2, and the fusion behavior-data from which the diagram was constructed are listed in table 3. It is seen that the compound ZrO_2-TiO_2 melts incongruently at about 1,820° C. The eutectic point for the system is located at about 80 mole percent TiO_2 and 1,760° C. Rather extensive solid-solution development is noted at the higher temperatures.

No attempt was made in this study to work out thoroughly the lower-temperature relationships in this system. Some observations on quenched specimens and slowly cooled specimens did, however, yield some information on this part of the system. X-ray analyses of specimens quenched from 1,500° C indicated that at this temperature about 12 percent of ZrO_2 will dissolve in TiO_2. This is in good agreement with the value given by Büssem, et al. (3).

TABLE 3. *Fusion characteristics of compositions in the* ZrO_2-TiO_2 *system*

Compositions				Results of heating		Results of petrographic or X-ray examination (specimens examined were not quenched and the phases observed may not be those in equilibrium at the liquidus)
Mole		Weight		Solidus	Liquidus	
ZrO_2	TiO_2	ZrO_2	TiO_2			
%	%	%	%	°C	°C	
90.00	10.00	93.28	6.72	----	----	Monoclinic ZrO_2 ss.
75.00	25.00	82.23	17.77	>1,900	----	Monoclinic ZrO_2 ss+ ZrO_2-TiO_2.
66.67	33.33	75.51	24.49	1,845	----	Do.
60.00	40.00	69.81	30.19	1,825	----	Do.
55.56	44.44	65.84	34.16	1,820	----	Do.
52.94	47.06	63.44	36.56	1,825	1,870	Do.
50.00	50.00	60.71	39.29	1,820	1,860	ZrO_2-TiO_2.
47.06	52.94	57.82	42.18	1,790	1,835	ZrO_2-TiO_2+TiO_2 ss.
44.44	55.56	55.23	44.77	1,775	1,820	Do.
40.00	60.00	50.69	49.31	1,760	1,825	Do.
33.33	66.67	43.54	56.46	1,755	1,800	Do.
25.00	75.00	33.95	66.05	1,765	1,780	Do.
20.00	80.00	27.83	72.17	1,755	1,760	Do.
16.67	83.33	23.57	76.43	1,760	1,780	Do.
10.00	90.00	14.63	85.37	1,785	1,805	TiO_2 ss.
5.00	95.00	7.51	92.49	1,810	1,830	Do.

The mole composition $2ZrO_2{:}3TiO_2$, when quenched from 1,460° C, had only a small percentage of TiO_2 in it, and the parameters of the $ZrO_2{\cdot}TiO_2$ had changed, indicating some solid solution at this temperature. No solid solution of TiO_2 in $ZrO_2{\cdot}TiO_2$ could be detected in slowly cooled samples.

Diffraction patterns of specimens high in ZrO_2 content indicated that TiO_2 is soluble in monoclinic ZrO_2 to the extent of 10 to 15 weight percent at room temperature. The ZrO_2 diffraction peaks in such samples had shifted to higher angles, indicating a smaller unit cell than that for pure ZrO_2. This result is at variance with the findings of Brown and Duwez [6], who stated that the solubility of titania in monoclinic ZrO_2 is probably very small.

5. The Compound $ZrO_2{\cdot}TiO_2$

In view of the disagreement between the present authors and some previous workers concerning the existence of the compound $ZrO_2{\cdot}TiO_2$, some discussion of its properties is in order. First of all, it was noted that the 1:1 mixture formed a single phase when fired at 1,250° C for a sufficiently long period of time, or when fired at higher temperatures for shorter periods of time. There is a superficial resemblance between the X-ray pattern of this material and that of tetragonal ZrO_2. However, the pattern of the 1:1 fired mixture contained so many excess lines that it could not be indexed on the basis of tetragonal symmetry. The patterns are compared in figure 3. It is evident that these patterns are for two entirely different materials.

Further, it was found that the 1:1 composition when fused and cooled relatively slowly, gave crystals large enough for petrographic examination. Such examination showed the material to consist of a single crystalline phase having the following properties: Biaxial (−), $2V \cong 80°$; approximate indices of refraction—$\alpha=2.33$, $\beta=2.38$, $\gamma=2.41$.

These properties are not compatible with tetragonal symmetry. It therefore must be assumed that the 1:1 mixture does not form stabilized tetragonal ZrO_2, but does form a distinct compound. It is to be noted that the X-ray pattern for the heated 1:1 mixture is indexed on the basis of orthorhombic symmetry. The indexed pattern is listed in table 4. The indexing of the powder pattern of $ZrO_2{\cdot}TiO_2$ was facilitated by the similarity of this pattern to that of tetragonal ZrO_2. It was noted that the 002/200 doublet of tetragonal ZrO_2 was split into three peaks, indicating a lower symmetry for $ZrO_2{\cdot}TiO_2$. When this triplet was assigned values of 002/020/200, the pattern was easily indexed and proved the compound $ZrO_2{\cdot}TiO_2$ to have orthorhombic symmetry.

The theoretical possibility of the formation of the compound $ZrO_2{\cdot}TiO_2$ may be realized by noting the work of Dietzal and Tober [17]. They state that the tendency for compound formation between two oxides is dependent upon the relative difference in the field strengths of the two components involved. The field strength may be represented as being proportional to the quantity z/a^2, where z is the charge on the cation, and a is the distance between the cation and anion. They noted that for most binary oxide systems $\Delta(z/a^2)$ should be at least 0.30 in order that compound formation may occur.

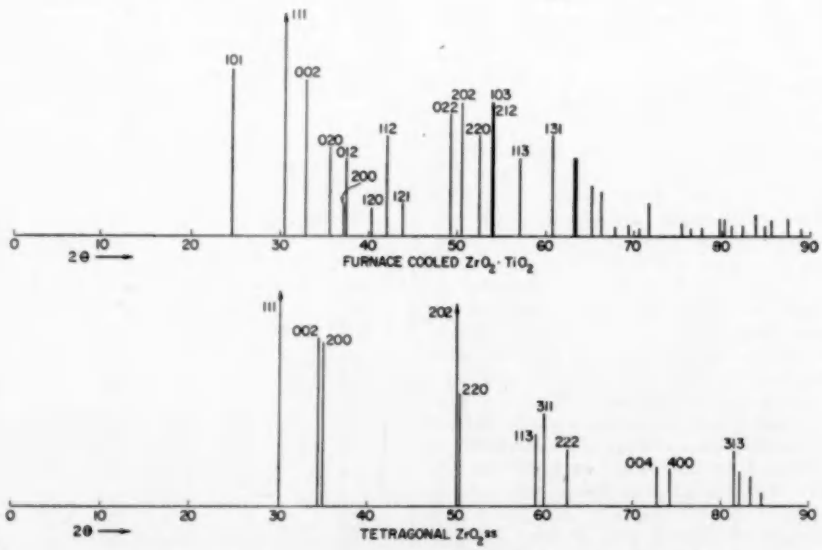

FIGURE 3. *X-ray diffraction patterns for* $ZrO_2{\cdot}TiO_2$ *and tetragonal* ZrO_2.

TABLE 4. *X-ray diffraction patterns of the compound* ZrO_2-TiO_2

Specimen slowly cooled from 1,550° C to room temperature				Specimen quenched from 1,550° C			
hkl	$1/d^2$ obs.	$1/d^2$ calc.	R. I.[a]	*hkl*	$1/d^2$ obs.	$1/d^2$ calc.	R. I.[a]
101	0.077	0.077	15	101	0.077	0.077	19
111	.117	.117	100	111	.116	.116	100
002	.135	.135	14	002	.133	.133	16
020	.158	.158	8	020	.158	.158	9
200	.173	.173	3	012	.173	.173	11
012	.174	.174	7	200	.173	.174	7
120	.201	.201	2.5	120	.201	.201	3
112	.218	.218	9	112	.216	.216	10
121	.235	.235	3	121	.235	.235	3
022	.293	.293	11	022	.291	.291	9
202	.308	.308	12	202	.307	.307	9
220	.331	.331	9	220	.332	.331	14
103	.347	.347	12	103	.343	.343	10
212	.348	.348	12	212	.346	.346	10
113	.386	.386	7	113	.382	.382	8
131	.433	.432	9	131	.432	.432	10
311	.463	.463	7	311	.462	.463	4
222	.465	.466	7	222	.465	.464	7
032	.490	.490	4.5	032	.489	.488	4
123	.505	.505	4	123	.501	.501	4
302	.525	.525	0.5				
320	.547	.547	1	320	.549	.548	0.5
312	.564	.564	0.5	014	.572	.572	3.5
014	.579	.579	3	321	.582	.581	.5
040	.632	.632	1	040	.632	.632	1
223	.647	.635	0.5				
033		.659					
232	.664	.663	.5	303	.689	.689	1.5
400	.693	.693	1.5	400	.693	.694	2
133	.7019	.7020	1.5	133	.6975	.6978	1.5
204	.7127	.7126	1	141	.7072	.7081	1
410	.7319	.7323	1	313	.7288	.7291	1
214	.7516	.7519	2	330	.7452	.7455	3
042	.7644	.7666	1	042	.7642	.7646	1
331	.7787	.7788	1.5	331	.7783	.7787	2
240	.8052	.8050	1.5	240	.8049	.8049	1
402	.8266	.8276	0.5	233	.8278	.8281	0.5
420	.8507	.8508	.5	323	.8473	.8475	1.5
412	.8692	.8671	2	224	.8655	.8636	0.5
224		.8704		412		.8663	
421	.8855	.8845	1	105	.8751	.8751	1
105		.8859		034	.8878	.8875	0.5
242	.9402	.9398	1	242	.9379	.9380	1
143	.9786	.9784	1	143	.9743	.9743	1
422	.9848	.9856	1	422	.9848	.9847	1
205	1.0140	1.0138	0.5				
150	1.0311	1.0305	1	413	1.0331	1.0330	2
125	1.0436	1.0438	1.5	333	1.0444	1.0445	0.5
430	1.0489	1.0482	1.5				
151	1.0652	1.0642	1	234	1.0615	1.0610	2
234	1.0683	1.0680	1	151	1.0634	1.0633	1.5
511	1.1551	1.1557	1	342	1.1552	1.1548	1
432	1.1829	1.1830	1	511		1.1568	
502	1.2201	1.2174	1	432	1.1812	1.1820	1
404		1.2320					
305	1.2319	1.2323	1	305	1.2220	1.2220	1
016	1.2524	1.2528	1				
521	1.2591	1.2568	1	016	1.2378	1.2371	0.5
414	1.2706	1.2716	1	414	1.2650	1.2656	1
343	1.3259	1.3245	1	252	1.3001	1.2932	0.5
244	1.3443	1.3442	1	343	1.3212	1.3212	1
441	1.3604	1.3583	0.5				
235		1.3711					
350	1.3773	1.3769	.5	325	1.3800	1.3798	1
424	1.3898	1.3900	1				
351	1.4101	1.4106	1	351	1.4109	1.4102	1.5
513	1.4255	1.4253	1	513	1.4288	1.4229	0.5
531	1.4706	1.4716	1	530		1.4393	
054	1.5263	1.5264	1	531	1.4726	1.4725	.5
				145	1.5071	1.5065	1
				054	1.5195	1.5190	1
				344	1.5534	1.5540	0.5
				434	1.5821	1.5813	.5

[a] R. I. is the intensity of diffraction peaks relative to the strongest peak.

Further, if compound formation does take place when $\Delta(z/a^2)$ is less than 0.30, the compound must have an incongruent melting point. Furthermore, they indicate that $\Delta(z/a^2)$ for the ZrO_2-TiO_2 system is equal to 0.30. Thus, we see that the compound ZrO_2-TiO_2 is a possible occurrence according to this scheme, and that, if formed, it should have incongruent melting characteristics. This is exactly the situation observed in the present study.

The compound when cooled slowly from a temperature of 1,200° to 1,600° C to room temperature has the following parameters: a=4.806A, b=5.032A, c=5.447A. If the compound is quenched from 1,200° to 1,500° C, the c-axis is found to have a larger value, whereas the a- and b-axes remain essentially the same. The parameters of the quenched compound are: a=4.802A, b=5.034A, c=5.483A. If the compound is quenched from 800° C, the parameters are the same as those in the slowly cooled specimen. These results seem to indicate the existence of two polymorphic forms of ZrO_2-TiO_2, with the transition temperature between 800° and 1,200° C.

The only extinction rules which are observed for the low temperature form of ZrO_2-TiO_2 are as follows; $h00$, $h=2n$; $0k0$, $k=2n$; $00l$, $l=2n$. From these it must be concluded that this compound has a primitive lattice rather than a face-centered lattice, as is the case in the tetragonal, cubic, and monoclinic forms of ZrO_2. The high-temperature form of ZrO_2-TiO_2 seems to have the additional extinction rule of: $h0l$, $h+l=2n$. This indicates that the high-temperature form of ZrO_2-TiO_2 has a different symmetry than the low-temperature form.

6. Summary

The systems CaO-TiO_2 and ZrO_2-TiO_2 were studied by observing solid-state reactions and fusion characteristics. The existence of two compounds in the CaO-TiO_2 system was confirmed. They are CaO·TiO_2, which melts congruently at about 1,915° C, and 3CaO·2TiO_2, which melts incongruently at about 1,750° C. The two eutectic points were located as follows: 75 mole percent TiO_2 and 1,475° C, and about 23 mole percent TiO_2 and 1,725° C. No solid-solution formation was noted in this system.

One compound, ZrO_2·TiO_2, was found to occur in the ZrO_2-TiO_2 system. This compound melts incongruently at about 1,820° C. The eutectic point for the system was located at about 80 mole percent TiO_2 and 1,760° C. Partial solid-solution development was noted in this system.

The X-ray powder diffraction pattern of the compound ZrO_2·TiO_2 was indexed on the basis of orthorhombic symmetry.

7. References

[1] Y. Tanaka, J. Chem. Soc. Japan **61,** 345 (1940).
[2] H. von Wartenberg, H. J. Reusch, and E. Saran, Z. anorg. u. allgem. Chem. **230,** 257 (1937).
[3] W. Büssem, C. Schusterius, and A. Ungewiss, Berg. deut. keram. Ges. **18,** 433 (1937).
[4] H. G. Sowman and A. I. Andrews, J. Am. Ceram. Soc. **34,** 298 (1951).
[5] Personal communication from Harold G. Sowman.
[6] Frank H. Brown and Pol Duwez, Progress Report 20–180, Jet Propulsion Laboratory, California Institute of Technology (August 20, 1952).

[7] R. F. Geller, P. J. Yavorsky, B. L. Steierman, and A. S. Creamer, J. Research NBS **36,** 277 (1946) RP1703.
[8] R. F. Geller, J. Research NBS **27,** 555 (1941) RP1443.
[9] S. M. Lang and R. F. Geller, J. Am. Ceram. Soc. **34,** 193 (1951).
[10] J. A. Hedvall and K. Anderson, Sci. Papers Inst. Phys. and Chem. Research (Tokyo) **38,** 210 (1941).
[11] I. Parga-Pondahl and K. Bergt, Tonind.-Ztg. **53,** 1000 (1933).
[12] L. D. Ershov, Trudy Giprotsementa, No. 1 (1940).
[13] P. S. Mamykin and B. A. Loshkarev, Ogneupory **15,** 215 (1950).
[14] H. G. Fisk, Jr., J. Am. Ceram. Soc. **34,** 9 (1951).
[15] R. C. De Vries, Rustum Roy, and E. F. Osborn, Paper presented at 1953 convention Am. Ceram. Soc. (April 28, 1953).
[16] H. von Wartenberg and W. Gurr, Z. anorg. u. allgem. Chem. **196,** 374 (1931).
[17] A. Dietzel and H. Tober, Ber. deut. keram. Ges. **30,** 71 (1953).

WASHINGTON, November 3, 1953.

Journal of Research of the National Bureau of Standards Vol. 52, No. 1, January 1954 Research Paper 2471

Conrady's Chromatic Condition[1]

Donald P. Feder

Nearly fifty years ago Conrady published a simple and ingenious formula for determining the state of chromatic correction of an optical system. This method, called the "*D-d* achromatism", depends upon the variation of the optical path as a function of wavelength. It can be used to evaluate both axial and lateral color, chromatic variation of spherical aberration, and secondary chromatic aberration. Unfortunately, this method is not as well known or as widely used as it deserves to be.

This paper proves the exact equation and discusses an extension of it which is approximate. A numerical example illustrates the accuracy obtainable with the approximation. The principal applications are presented and formulas derived giving the relations between the "*D-d* method" and conventional means of expressing the chromatic aberration.

1. Introduction

Professor Conrady is among the best-known teachers of the art of optical design. His book "Applied optics and optical design" is familiar to most designers and is a bible to some. The "*D-d* method" for calculating chromatic aberration, however, is not found in his book, and this may account for the fact that it is not as widely known as it deserves to be. The method was published in two papers in the Monthly Notices of the Royal Astronomical Society nearly fifty years ago.[2] It was surprising to find recently that many good lens designers are unacquainted with the method. Furthermore, even those who use it do not often apply it to off-axis imagery.

It will be shown in this paper, that after rays have been traced through the system to determine the monochromatic aberrations, the complete state of the chromatic correction can then be found with very little extra work and without the necessity of tracing rays at any other wavelength. In addition the *D-d* method gives the results of ray tracing at three wavelengths. Because this method gives answers in the form of optical path differences, it is frequently easier to obtain a well corrected system by this method than by conventional methods. The use of the *D-d* method is recommended to designers who require a simple and elegant way for finding the chromatic aberration of an optical system over the entire field.

The proof presented by Conrady is not entirely satisfactory, and later proofs, although more cumbersome, are less convincing. Some of them depend upon very complicated geometrical figures that are difficult to follow.

The region of validity of the formula is not well defined. A recent paper, for example, stated that the chromatic variation of spherical aberration is not always given correctly by the formula. Conrady, himself, appeared to think that the secondary chromatic aberration[3] was exactly determined by the *D-d* method. It will be seen below, however, that any aberration determined by the first derivative with respect to wavelength is precisely given by this formula. Therefore, any chromatic aberration, including chromatic variation of spherical, is accurately given over a narrow wavelength region in the neighborhood of the median wavelength *no matter what the monochromatic aberrations of the system may be*. For a somewhat wider wavelength region the method gives an approximate answer, which is ordinarily good enough to determine the secondary chromatic aberration of the system.

2. Derivation of Principal Equation

Figure 1 shows a meridan section through a typical lens. The proof will be given for this case and immediately extended to any number of elements. A point source at O is emitting light that is refracted by the lens. For a particular wavelength λ_0, we consider a wave front in the image space. We may suppose that this wave front is located a considerable distance from the image of O. We take a point, P, lying on the wave front, and draw the normal to the wave front. This normal coincides with a ray in the image space whose extension in the object space passes through O. This ray is shown as a solid line in figure 1. In like manner for any wavelength λ, there exists a unique ray passing from O to P. Another such ray is shown by the dotted line in figure 1.

In order to find the chromatic aberration, we should like to know what happens to the wave front when the wavelength is varied. We first consider what happens at the point P, and then, by letting P move over the wave front, obtain the total effect. We first mark off along the ray the distances D_1, D_2, D_3, D_4 intercepted on the ray by the various media. The distance D_4 is the distance along the ray from the last surface to the point P. As the wave-

[1] This work was done as part of a research project sponsored by the U. S. Air Force.

[2] A. E. Conrady, Monthly Notices of the Royal Astronomical Society, p. 182 (Jan. 1904); p. 458 (March 1904).

[3] Because of strong objections by some people to the term *secondary spectrum*, the expression *secondary chromatic aberration* is used for this quantity throughout the paper.

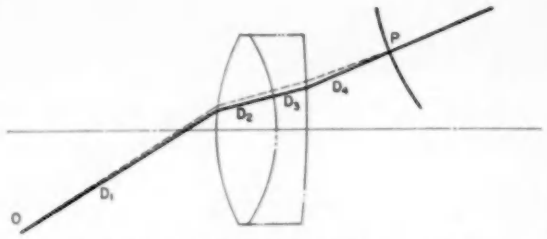

FIGURE 1. *Meridian section of typical lens.*

Light from a point source at O traverses a typical lens producing an emergent wave front at P in light of wavelength λ_0. The solid line shows such a ray with the distances in the various media indicated by D_1, D_2, D_3, D_4. The dotted line indicates a ray going from O to P for another wavelength λ. The wave front for λ is not shown in the figure.

length changes, the distances D_1, D_2, D_3, D_4, change and so are to be considered functions of λ.

Let us define $V(\lambda)$ to be the optical-path length from O to P. Suppose, for convenience, that the object and image are in air; then

$$V(\lambda)=D_1+N_2D_2+N_3D_3+D_4,$$

where N_1 and N_2 are the refractive indices of the corresponding media. Differentiating V with respect to λ gives the rate of change of the optical-path length from O to P. One obtains

$$\frac{dV}{d\lambda}=\left\{\frac{dD_1}{d\lambda}+N_2\frac{dD_2}{d\lambda}+N_3\frac{dD_3}{d\lambda}+\frac{dD_4}{d\lambda}\right\}+\left\{\frac{dN_2}{d\lambda}D_2+\frac{dN_3}{d\lambda}D_3\right\}.$$

One sees that the derivative is divided naturally into two parts. In the first part (left-hand bracket), the refractive indices are held fixed. Therefore, this part results from the variation of the path of the ray and is zero by Fermat's principle.

Fermat's principle states that the optical-path length between two fixed points possesses a stationary value with respect to arbitrary variations of the mechanical path. In this case we are considering a subset of all the possible variations in path from O to P: namely, only such variations as are generated by varying λ. Because of the manner in which this subset was chosen, it is clear that it contains, for light of any fixed wavelength λ, the actual path traversed by the light. Furthermore, for light of this wavelength λ, the actual path possesses a stationary value. In mathematical language,

$$dD_1/d\lambda+N_2dD_2/d\lambda+N_3dD_3/d\lambda+dD_4/d\lambda=O.$$

It follows that $dV/d\lambda=D_2dN_2/d\lambda+D_3dN_3/d\lambda$. This equation can be immediately generalized to any number of elements giving

$$\frac{dV}{d\lambda}=\sum\frac{dN}{d\lambda}D. \qquad (1)$$

This is the principal equation, and forms the basis for the method. It should be noted that nothing in its derivation restricts its application to axial object points or even to meridian rays.

2.1. Significance of Principal Equation

To understand the significance of eq (1) recall that for light of a fixed wavelength, the optical-path length, V, from the object point to any point on the wave front is a constant. Suppose that $dV/d\lambda$ has been calculated for all points P on the wave front of wavelength λ. For a sufficiently small increment in wavelength, $\Delta\lambda$, it is approximately true that $\Delta V=(dV/d\lambda)\Delta\lambda$. A point P' is now defined such that P' lies on the ray through P, and such that the displacement of P' from P is $-\Delta V$. It is clear that the optical-path length V' from O to P' for light of wavelength $\lambda+\Delta\lambda$ is equal to V. In this manner a set of points P' is constructed, which constitutes a wave front for light of wavelength $\lambda+\Delta\lambda$. By the nature of the construction, the displacement of this wave front from the original wave front is $-(dV/d\lambda)\Delta\lambda$. This equation becomes exact only in the limit as $\Delta\lambda\to 0$.

The above argument shows that if ΔV is a constant over the entire wave front, then the changed wave front is "parallel" to the original one, and there is no chromatic aberration in the image of O. Stated more precisely, if $dV/d\lambda$, evaluated at $\lambda=\lambda_0$, is the same at all points on the wave front, there is no chromatic aberration in the wavelength region around λ_0. On the other hand, the variation of $dV/d\lambda$, as P is moved over the wave front, is a measure of the chromatic aberration. A more detailed study of this point is given later in this paper.

The actual calculation of $dV/d\lambda$ from eq (1) is a simple matter. After the monochromatic errors are determined by tracing rays at a central wavelength, the values of the D's are available as a byproduct. The quantities $dN/d\lambda$ are available from the known properties of the glasses employed. It is a simple matter to form the indicated sum for several points on the wave front and to examine the chromatic aberration in the vicinity of the central wavelength

2.2. The Approximate Equation

Now one may ask how to determine the secondary chromatic aberration. For this it is necessary to calculate $d^2V/d\lambda^2$. As eq (1) holds for all values of λ, it may be differentiated, yielding

$$d^2V/d\lambda^2=\Sigma Dd^2V/d\lambda^2+\Sigma(dN/d\lambda)(dD/d\lambda). \qquad (2)$$

The first term of eq (2) is easy to obtain, but the second term is more troublesome. Unfortunately, it is not zero, but computations on several widely different systems show that it must be considerably smaller than the term $\Sigma Dd^2N/d\lambda^2$. If this term, and all terms of higher order in $\Delta\lambda$, are neglected, then one has

$$\Delta V=\frac{dV}{d\lambda}\Delta\lambda+\frac{d^2V}{d\lambda^2}\frac{(\Delta\lambda)^2}{2}=\Sigma D\left\{\frac{dN}{d\lambda}\Delta\lambda+\frac{d^2N}{d\lambda^2}\frac{(\Delta\lambda)^2}{2}\right\},$$

originally,

$$\Delta V = \Sigma D \Delta N. \tag{3}$$

Equation (3) is an approximate equation, but it gives more information than eq (1) because it takes partial account of all higher derivatives of N with respect to λ. Furthermore, it is much easier to apply than eq (1) because the glass catalogs list the indices for discrete wavelengths, and in many cases list the values of ΔN directly. On the other hand, in order to find $dN/d\lambda$ for use in eq (1) it is necessary to fit one of the various dispersion formulas to the glass data and to compute $dN/d\lambda$ for the wavelength at which the rays were traced. Although this is a straightforward procedure, and has the advantage of being mathematically exact, the use of eq (3) not only entails less work but also gives an approximate idea of the secondary chromatic aberration.

2.3. Modification When Final Medium Is Not Air

In the case that the final image is not formed in air, then $-\Delta V/N'$ rather than $-\Delta V$ is the correct expression for the displacement of the wave front. Here N' is the index of the final medium.

It must also be remembered that the sum $\Sigma D \Delta N$ should include the term $D' \Delta N'$ for the last medium, where D' is the distance along the ray from the last refracting surface to the focal surface.

3. Application of Method

After rays have been traced through the system to determine the monochromatic errors, it is necessary to determine the D's in each medium for which $\Delta N \neq 0$. Fortunately, in the usual lens there are several air spaces (where $\Delta N = 0$), and these disappear from the summation in eq (3). In some ray-tracing schemes the values of the D's are immediately available for each medium, and in others these quantities are not directly given. Even in the latter event, however, they can easily be computed from the ray-tracing data. A common method for meridian rays employs the angle of incidence, I, and the angle of inclination, U, as coordinates of the ray. In this case one has

$$D = r_1 \cos I_1' - r_2 \cos I_2 + (t_{12} - r_1 + r_2) \cos U_{12},$$

where I_1' is the angle of refraction and r_1 the radius of the surface preceding the medium; I_2 is the angle of incidence, and r_2 is the radius of the surface following the medium, and U_{12} is the angle of inclination of the ray in the medium of thickness t_{12}.

The values of the D's need not be obtained with high precision because each D is multiplied by a small number, which is rarely larger than 0.03. This is an important point from the standpoint of the practical computer. Five place accuracy in the D's is more than sufficient for even the most precise work.

After the values of the D's have been computed by any suitable method, one forms for each traced ray the sum $\Sigma D \Delta N = \Delta V$. If one is achromatizing for the region from F to C, then $N_F - N_C$ for ΔN is used. Then ΔV is plotted against some variable that is a measure of the position of the ray in the aperture. For meridian rays this variable may be the coordinate of the ray in the entrance pupil, the tangent of the slope angle of the image ray, or any variable that locates the ray in the aperture. For reasons of convenience, which will appear later, we shall use in this paper sin U, where U is the angle of inclination of the image ray.

3.1. Interpretation

a. Axial Object Points

If, for the axial bundle of rays, one plots the value of ΔV against sin U, a curve that is symmetrical about the line sin $U = 0$ is obtained. The displacement of the curve is immaterial, and it is customary to subtract from each ordinate the value of ΔV at the origin. This value is $\Sigma d \Delta N$, where d is the axial distance between surfaces. One obtains $\Sigma(D-d)\Delta N$, and this is plotted against sin U. This is the formula that gives rise to the popular name for the method, the $D-d$ method.

If the lens has no longitudinal chromatic aberration, the curve will be a straight line (see fig. 2). If simple primary aberration is present, the curve will be approximately parabolic and will be concave upward in the case of overcorrection and concave downward for undercorrection. (In establishing a sign convention, ΔN is taken to be positive for all the media, and sin U is taken to be positive when the final ray slopes downward to the right. It should be noted that if ΔV is positive, the wave front for $\lambda + \Delta\lambda$ is *behind* the wave front for λ.) A simple relation between the curvature of the parabola and the longitudinal aberration is derived in the final section.

Usually the situation is complicated by the presence of chromatic variation of spherical aberration. In many lenses initial undercorrection is followed by marginal overcorrection producing a zone. A case of this type is shown in figure 2. Good correc-

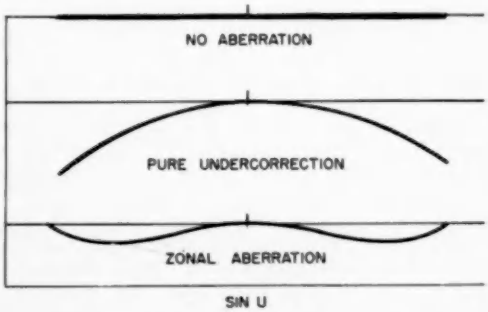

FIGURE 2. *Axial fan.*

The ordinate for each curve is $\Sigma(D-d)\Delta N$. As these curves are for axial points, they are necessarily symmetrical about the line sin $U = 0$.

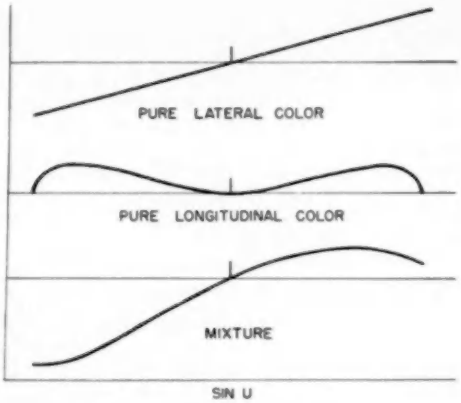

FIGURE 3. *Oblique fan.*

The ordinate for each curve is ΔV. Because the displacement is of no importance, each curve can be zeroed about the chief ray. If the curve shows symmetry about the value of sin U corresponding to the chief ray, then only pure longitudinal color is present. A tilt indicates lateral color.

tion here makes $\Sigma(D-d)\Delta N=0$ at the margin. Then wave fronts that are tangent in the center of the aperture will cross at the margin. At a point usually near the 0.7 zone the wave fronts will be parallel and the corresponding rays coincident.

b. Extra-Axial Object Points

As mentioned above, for meridian rays one plots ΔV against sin U, where U is the slope angle of the final ray in the image space and $\Delta V=\Sigma D\Delta N$. In this case, the symmetry present on axis is no longer inherent. Figure 3 depicts some of the characteristic types of chromatic aberration that may be present in oblique bundles. If the curve is a straight line inclined to the sin U axis, then pure lateral aberration is present. One may think of the wave fronts as being inclined to one another. The lateral aberration is proportional to the slope of the line, and its numerical value can readily be obtained (see section 3.3). As before the displacement of the curve is immaterial, only the differences in ΔV being significant. If the curve is symmetrical about a line parallel to the ΔV axis through the chief ray, then pure longitudinal aberration is present. The longitudinal aberration for an off-axis object point may be quite different from that present on the axis.

In the ordinary case the curve possesses neither symmetry nor straightness, and the aberration is a mixture of lateral and longitudinal chromatic aberration.

In the final stages of an optical design, one may have curves of ΔV against sin U for several different object points. It is desirable to obtain the best correction throughout the usable field. An advantage of this method is that the chromatic aberration is represented in the same manner both on and off axis.

The skew-ray aberration is also represented by ΔV, and in some cases it may be desirable to at least plot the sagittal rays. The author believes, however, that the chromatic aberration of the skew rays will not be troublesome if the meridian rays are properly corrected.

c. Secondary chromatic aberration

To obtain an estimate of the secondary chromatic aberration, one should recompute ΔV by using a different set of ΔN. Suppose, for example, that the central wavelength is sodium D and that rays have been traced in this color to determine the monochromatic aberrations. It is desired to correct the lens in the spectral region C to F. The procedure might be as follows:

1. The sum $\Sigma(D-d)\Delta N$ is made zero at the margin using N_F-N_C for ΔN and using the values of the D's obtained from ray tracing in sodium light.

2. Check $\Sigma(D-d)\Delta N$ to make sure that it is satisfactory over the whole aperture. There is no point in worrying about the secondary chromatic aberration if there is a large amount of chromatic variation of spherical aberration present.

3. After $\Sigma(D-d)\Delta N$ is satisfactory over the aperture, it can be recomputed by using the value N_F-N_D for ΔN and the same values for the D's as before. The value of this second sum is an indication of the secondary chromatic aberration. There will be some error owing to the fact that eq (3) involves an approximation, but this is not serious for most purposes.

It should be recognized that the important use of the D-d method is to calculate the higher order chromatic aberrations. Before applying this method, a competent designer will already know the primary values of the longitudinal and lateral color and will have reduced these aberrations to reasonably small values.

If the secondary chromatic aberration is to be corrected, it must first be approximately corrected in the paraxial region. The simplest way to determine this is by tracing paraxial rays for the separate wavelengths. After paraxial correction is made, it is necessary to apply the D-d method as listed in steps 1, 2, and 3 above to ascertain whether good correction has been achieved over the entire aperture.

3.2. Tolerances

One can set up a tolerance for the variation of ΔV on the basis of physical optics. Suppose that the image in D light is sharp and that ΔV calculated from F to D does not vary more than one-fourth wave over the aperture. Then at the D focus the image in F light will be sensibly perfect within the meaning of the Rayleigh limit. Similarly, if the variation in ΔV calculated from D to C is also less than one-fourth wave, then the image in C light observed at the D focus will be sharp. Under such circumstances the chromatic aberration would be extremely well corrected over the entire region from F to C. On the other hand, the above tolerance is extremely strict and will seldom be met in practice. Usually one corrects the axial bundle of rays so that $\Sigma(D-d)\Delta N$

is zero at the edge of the aperture, and this correction is ordinarily quite adequate. If there is a large zone because of the presence of chromatic variation of spherical aberration, then a basic change in the design is necessary to reduce this aberration. If the secondary chromatic aberration is to be corrected, provision for this correction must be made in the preliminary design.

In lenses covering an appreciable field, the curves for several obliquities must be simultaneously corrected, and this may lead to sacrificing best axial correction in order to gain at the edge of the field. The *D-d* method is ideally suited to making such decisions because the chromatic aberration from axial and extra-axial object points are both represented by the same type of graph.

In very many cases the tolerances are determined by a combination of experience and such overriding considerations as cost and complexity.

3.3 Relation Between Ray and Wave-Front Aberrations

For designers who are more familiar with ray-intercept methods for expressing chromatic aberration, it should be helpful to have a formula relating one to the other. Such a formula is derived below for meridian rays.

One considers a wave front in light of wavelength λ located a distance R from the focal plane (see fig. 4). When the wavelength is changed by $\Delta\lambda$, the changed wave front makes an angle δ with the original wave front at some arbitrary point P. It is clear that $d(\Delta V)/ds=\delta$, where s is the arc length measured along the wave front. Also $s=RU$ because the wave front is nearly spherical. (Here U is the angle of inclination that the final ray makes with the optical axis.) Now one has

$$\Delta y=\frac{R\delta}{\cos U}=\frac{R}{\cos U}\left\{\frac{d(\Delta V)}{ds}\right\} \quad \text{and} \quad ds=R\,dU.$$

Then

$$\Delta y=\frac{R}{\cos U}\left\{\frac{d(\Delta V)}{R\,dU}\right\}=\frac{1}{\cos U}\,\frac{d(\Delta V)}{dU}.$$

Finally,

$$\Delta y=\frac{d(\Delta V)}{d(\sin U)}. \tag{4}$$

The existence of eq (4) is the reason for plotting ΔV against sin U rather than against some other aperture variable, such as tan U.

Equation (4) gives the displacement of the ray because of a change in λ. One can plot ΔV against sin U for several traced rays. By measuring the slope of the curve at any point, one finds the displacement between rays in the two wavelengths at that point. Using the formula, one can obtain the ray-intercept curve for any other wavelength after the curve has been found in the central wavelength. In practice, however, it is not usually desirable to do this because the single curve of ΔV against sin U is easier to interpret than two ray-intercept curves for different wavelengths.

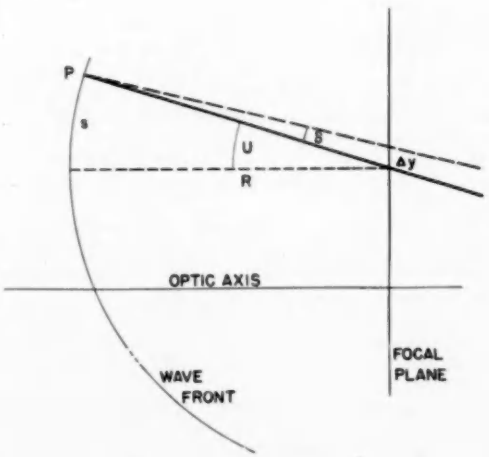

FIGURE 4.

The full curve shows a wave front in light of wavelength λ located a distance R from the focus. A ray normal to this wave front at P makes an angle U with the optic axis. A ray in light of wavelength $\lambda+\Delta\lambda$ makes an angle δ with the first ray. It is indicated by a dotted line through P crossing the focal plane at a distance Δy from the first ray.

3.4. Numerical Example

Figure 5,a, shows a curve obtained in an actual lens design. It represents the monochromatic aber-

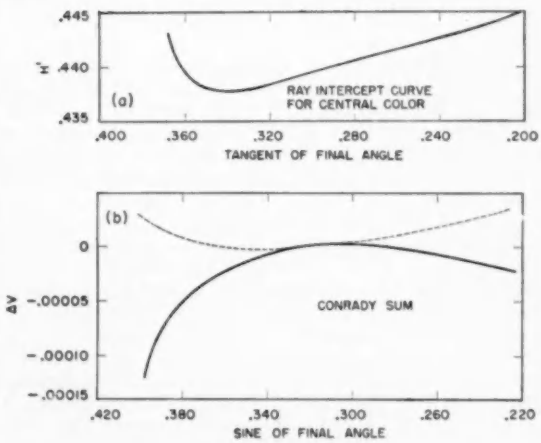

FIGURE 5.

(a) The upper curve shows the meridian ray aberration at 60° obliquity from the axis in *D* light. The ordinate H' is the height of the ray on the focal plane, the abscissa is the tangent of the final angle. (b) The lower curves show ΔV for the same lens at the same obliquity. The solid curve is for the wave length region *F* to *D*; the dotted curve from *C* to *D*.

These curves show the ray intercept curves at 60° in *F* light (solid line) and *C* light (dotted line) predicted by equation (4) from the curves in figure 5. The crosses show the actual results of ray tracing in F light (solid curve) and the circles the results of ray tracing in *C* light (dotted curve).

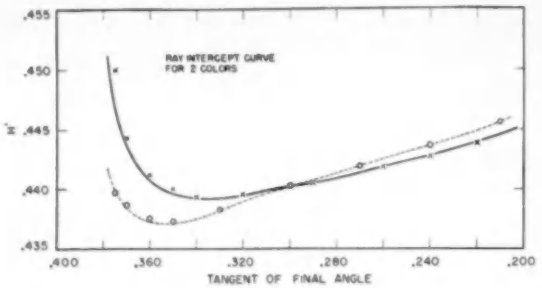

FIGURE 6. *Ray-intercept curve for two colors.*

ration for D light for an object point 60° from the optic axis. This lens was a complex system containing aspheric surfaces and was in an early stage of design. Figure 5,b, shows the curve of ΔV from F to D and the curve of ΔV from C to D. Normally one would plot only the difference (that is, ΔV from F to C), but in this case the ray-intercept curves for all three wavelengths were desired. From the slope of these curves, the values of Δy have been calculated by eq (4). These differences were then added to the curve in figure 5,a, to obtain the curves in figure 6 and these curves checked by ray tracing. The crosses and circles show the position of the traced rays. The agreement is good except on the left end, where the aberration is large. The discrepancy is due to the fact that the wavelength interval used is not sufficiently small.

3.5. Paraxial Correspondence

One might ask the question how the curve for $\Sigma(D-d)\Delta N$ against aperture is related to the paraxial chromatic aberration. It would be possible to find this correspondence by an investigation of the limiting behavior of $\Sigma(D-d)\Delta N$ as the aperture is reduced to zero. Such an investigation, however, could only produce a well known formula giving the value of the longitudinal aberration in terms of the paraxial ray tracing data. This formula is reproduced below for reference.

Instead of deriving this formula from an optical path difference standpoint however, we shall attack the problem in a different manner, that is, by assuming that the longitudinal aberration is known and determining $\Sigma(D-d)\Delta N$ by using this information. Suppose there is a longitudinal difference in focus δl between the image positions for two wavelengths. In the neighborhood of the axis each wave front is a sphere centered about its focus. Consider a fixed point on the axis, well removed from the focus, and the two spherical wave fronts passing through this point (see fig. 7). We ask the question, how does the distance between these spheres behave as a function of aperture?

If x and y are the coordinates of a point on the

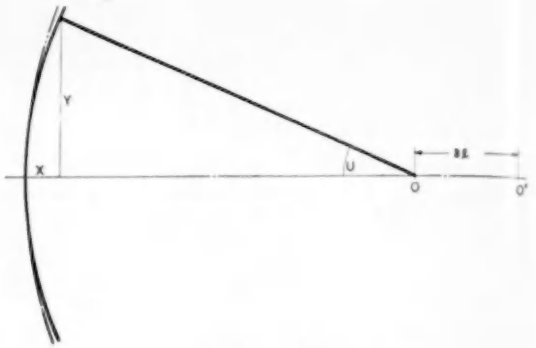

FIGURE 7.

Two wave fronts in light of different colors in the neighborhood of the axis. The longitudinal abberration is δl. The wave front separation is Δr.

sphere of radius r, then $x=\frac{1}{2}y^2r^{-1}$ is valid for a meridian section in the neighborhood of the axis, where r is the radius. The x-axis coincides with the optical axis, and $x=0$ at the vertex of the sphere. Differentiating with respect to r, one has $\Delta x=-\frac{1}{2}y^2r^{-2}\Delta r$ as the approximate displacement of the sphere of radius $r+\Delta r$ from the sphere of radius r. But $\Delta x=-\Delta V/N'$, where $\Delta V=\Sigma D\Delta N$ and N' is the final index (see eq (3), section 2). Then $\Delta V=\frac{1}{2}N'y^2r^{-2}\,\delta l$, since $\delta l=\Delta r$. Also $\sin U=yr^{-1}$, and so

$$\Delta V=\tfrac{1}{2}N'\delta l\sin^2 U. \tag{5}$$

Equation (5) shows that the curve of ΔV against $\sin U$ is a circle or parabola for small values of U and that the curvature is $N'\delta l$. This then is the paraxial correspondence desired. Another way of expressing this result is to consider ΔV as a power series in $\sin U$. For an axial object point this series has the form $\Delta V=c_0+c_2\sin^2 U+c_4\sin^4 U+\ldots$. The odd powers of $\sin U$ are absent because of symmetry. The first term c_0 is of no importance because it only represents a displacement of the reference point, which indicates that the wave fronts for the two wavelengths do not pass through the same axial point. This term c_0 is similar to the quantity $\Sigma d\Delta N$, which it is customary to subtract from ΔV.

The coefficient c_2 depends upon the paraxial difference in focus, and by eq (5) $c_2=\frac{1}{2}N'\delta l$. The coefficients c_4, c_6, etc. are related to the chromatic difference in spherical aberration. It might be emphasized that the D-d method gives the sum of this series precisely for small wavelength variations and approximately for finite differences in wavelength.

In practice, the designer determines δl either exactly from a paraxial ray trace, or approximately by a formula given below. Then ΔV is determined from the $D-d$ method for a number of points throughout the aperture. (Frequently the values at

the margin and the 0.7 zone are sufficient.) Then a curve can be drawn for ΔV versus sin U by making use of the value of δl to draw the curve near the origin. The curves shown in figure 2 were obtained in this manner.

The approximate formula for δl is

$$\delta l = a(N'u^2)^{-1} \tag{6}$$

where

$$a = \sum_k y_k i_k (\Delta N_k - \mu_k \Delta N_k').$$

The meanings of the above symbols, which all refer to the paraxial ray, are as follows:

u is the paraxial inclination angle in the final medium.

y is the height of incidence.

$\mu = N/N'$ at the refractive surface.

ΔN and $\Delta N'$ are the differences in indices for two wavelengths for the media preceding and following the refracting surface.

The subscript k refers to the kth surface and the sum runs over all the refracting surfaces in the system, the expression $(N'u^2)^{-1}$ refers to the final medium.

Combining eq (6) with eq (5), one finds that $\Delta V = \frac{1}{2}a$ if one takes sin $U = u$. This means that if one traces a paraxial ray through the system and computes a by eq (6), then ΔV along this ray is simply $\frac{1}{2}a$.

WASHINGTON, July 15, 1953.

U. S. GOVERNMENT PRINTING OFFICE: 1954